LBL-31160
Preprint

Lawrence Berkeley Laboratory
UNIVERSITY OF CALIFORNIA

APPLIED SCIENCE DIVISION

Submitted to Environmental Science and Technology

Influence of Subslab Aggregate Permeability on SSV Performance

A.J. Gadgil, Y.C. Bonnefous, W.J. Fisk, R.J. Prill, and A. Nematollahi

September 1991

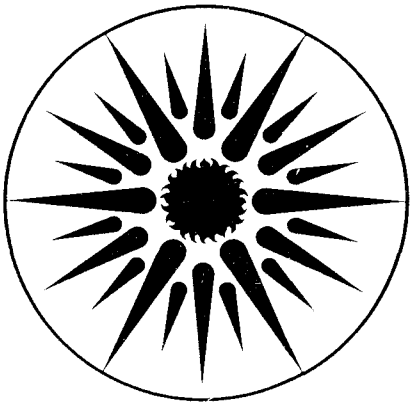

APPLIED SCIENCE DIVISION

Prepared for the U.S. Department of Energy under Contract Number DE-AC03-76SF00098

To be submitted to E.S. & T. without appendices.

Influence of Subslab Aggregate Permeability On SSV Performance

Final Report

Gadgil, A.J., Bonnefous, Y.C., Fisk, W.J., Prill, R.J.[*], *and Nematollahi, A.*
Indoor Environment Program, Lawrence Berkeley Laboratory
Berkeley, California

and

[*]Washington State Energy Office
Washington Energy Extension Service
Spokane, Washington

September 1991

This research was supported at Indoor Program of Lawrence Berkeley Laboratory by Bonneville Power Administration (BPA) through interagency agreement DE-AI79-90BP06649, and by the Assistant Secretary for Conservation and Renewable Energy, Office of Building Technologies, Building Systems and Materials Division of the U.S. Department of Energy under Contract DE-AC03-76SF00098. This research was also supported at Washington State Energy Office, Energy Extension Service by BPA Coop Agreement DE-FC79-82BO34623 Modification AO27 (WSE) 90-04). Partial support for Yves Bonnefous's research participation was granted by ENTPE of Lyon, France.

Abstract

The effectiveness of the technique of subslab ventilation (SSV) for limiting radon entry into basements was investigated through complementary experimentation and numerical modeling. Determination of the impact of subslab aggregate permeability on SSV performance was a primary objective. Subslab pressure fields resulting from SSV were measured in six well-characterized basements, each with a different combination of soil and aggregate permeability. The relationship between air velocity and pressure gradient within the three types of aggregate installed beneath the basement slabs was measured in the laboratory. A new numerical model of SSV was developed and verified with the field data. This model simulates non-Darcy flow in the aggregate. We demonstrate that non-Darcy effects significantly impact SSV performance. Field data and numerical simulations indicate that increasing the aggregate permeability within the investigated range of $2.x10^{-8}\,m^2$ to $3.x10^{-7}\,m^2$ substantially improves the extension of the subslab pressure field due to SSV operation. Subslab pressure field extension also improves as soil permeability decreases between $10^{-9}\,m^2$ and $10^{-10}\,m^2$. With a slab-wall gap thickness of 1 mm and the range of aggregate permeability investigated, further reductions in soil permeability do not significantly improve the subslab pressure field extension. Sealing of cracks in the slab and excavation of a small pit where the SSV pipe penetrates the slab also dramatically improve this pressure field extension. A large ratio of aggregate permeability to soil permeability reduces the need for large depressurizations at the SSV pit. Our findings are consistent with the results of prior field studies; however, our understanding of SSV is improved and the dependence of SSV performance on the relevant parameters can now be quantified with the model.

1. Background

Within the U.S., exposure to the radioactive decay products of radon (^{222}Rn) in buildings is the most important source of human exposure to environmental radiation and also one of the largest sources of risk to human health caused by an indoor pollutant (Nazaroff and Nero 1988). In houses with elevated indoor Rn concentrations, the primary source of Rn is usually the surrounding soil where Rn is generated by the radioactive decay of trace amounts of radium. The predominant process of Rn entry into these houses is pressure driven flow of high-Rn soil gas into the structure through small cracks, joints and holes.

Subslab ventilation (SSV) is one of the most effective and common methods of reducing indoor Rn concentrations in houses with basements. There are two basic methods of SSV (Turk et al 1989). In subslab depressurization (SSD), a fan exhausts soil gas from beneath the slab floor to the outside. The fan usually draws air through one or more plastic pipes that penetrate the slab floor. This process decreases the pressure beneath the floor and, therefore, reverses the pressure difference that normally causes soil gas and Rn to flow into the structure. Passive SSD systems that utilize vertical stacks passing through the heated interior of buildings (in place of the fans) are currently being investigated. In subslab pressurization (SSP), outdoor air is forced beneath the slab using a fan (i.e., the direction of air flow is reversed compared to that in a SSD system). SSP ventilates the soil beneath the slab floor, thus reducing radon concentrations within the soil near the slab. Soil gas entry into the structure continues, but the concentration of Rn in the entering soil gas is decreased.

SSV has become a widely used Rn control measure. During construction of new houses, provisions that increase the effectiveness or ease the installation of SSV systems are sometimes recommended or required by code. The most common provision is a layer of highly permeable (clean and coarse) aggregate beneath the slab floor. Based primarily on our general understanding of flow through permeable media and informal evidence from field studies of SSV, a high permeability aggregate layer improves the extension of the pressure field beneath the slab caused by SSV operation (i.e., the high permeability aggregate results in a smaller decrease in the magnitude of depressurization or pressurization with distance from the point of air withdrawal or supply).

The U.S. Environmental Protection Agency (EPA 1991) recommends installation of a 10 cm-thick layer of aggregate "with a minimum of 80% of the aggregate at least 3/4 inch in diameter" beneath slab floors to facilitate SSV in case it is needed. Similarly, a Washington State Ventilation and Indoor Air Quality Code (WSBCC 1990) and a Model Northwest Residential Radon Standard (Nuess 1989) require installation of clean coarse aggregate layer in some situations (clean and coarse are defined through aggregate specifications).

Claims of improved SSV performance due to the presence of continuous subslab aggregate layers (compared to no aggregate) are rarely debated. For example, Furman and Hintenlang (1990) show that a layer of aggregate located above sand clearly improves pressure field extension beneath test slabs. However, the impact of aggregate type (e.g., permeability) on SSV performance is controversial and is also the primary focus of this paper. Some relevant information has been previously published. Matthews et al. (1988) present a closed form model for cylindrical flow in a subslab aggregate layer (flow through the soil or through cracks in the slab are neglected). They use experimental data on pressure field extension to determine the value of constants within the model, and report a good correlation between measurements and predictions. The final model indicates that air velocity within the aggregate (during their experiments) is approximately proportional to the pressure gradient raised to the 0.7 power and that pressure field extension will improve with increased aggregate permeability. In 1989, Barber presented a numerical model of SSV in Florida-style slab on grade housing with sand (but not aggregate) located beneath the slab. As shown later, a model of Darcy flow is not adequate for simulations of SSV performance when aggregate is located beneath the slab.

A recently published paper by Gadsby et al. (1991) focuses specifically on SSV performance as a function of aggregate type. In the laboratory, they studied air velocity (V) versus pressure gradient ($\frac{dP}{dx}$) in four different types of aggregate. They do not assume Darcy flow, instead they employ a power-law expression of the form

$$\frac{dP}{dx} \alpha (1/K_g) V^b$$

where K_g is the aggregate permeability and b is an exponent, both determined experimentally. The experimental data are used in a closed-form model that approximately emulates the condition of aggregate located between a basement floor and soil. The assumed geometry is a cylindrical layer of aggregate surrounded by a larger diameter hollow cylinder of soil (which represents the soil adjacent to the basement walls), both located between two impermeable circular disks. Flow occurs in the radial direction toward a central suction point. The major limitations of this model, other than the simplified geometry, are that flow through cracks in the slab and through the soil beneath the aggregate are neglected. Based on this model and the measured aggregate data, the authors conclude that pressure field extension is more dependent on soil permeability than aggregate permeability.

The research described in this paper represents an additional advance in both experimental assessment and modeling of SSV performance as will be described in the subsequent sections.

2. Objectives and Overall Approach

2.1 Objectives

The primary objective of this research was to determine quantitatively the influence of subslab aggregate type on the performance of SSV systems. Secondary objectives are to develop a more complete model of SSV and to investigate SSV performance as a function of selected SSV system parameters, building substructure, and soil characteristics (such as the magnitude of the depressurization at the suction point, the size and location of cracks in the slab, and the permeability of the soil).

2.2 Overall Approach

The research approach involves coordinated data collection in new houses located in the Spokane, WA area, laboratory characterization of flow through aggregate samples obtained from these house sites, and numerical modeling.

2.2.1 Field Experiments

Six houses with basements were selected for field measurements. The criteria for site and house selection were: relatively homogeneous soil, level or simply sloping ground surface, large variability in soil permeability between sites, and a relatively simple basement geometry. The houses were built with one of three types of aggregate beneath the slab floor, thus, each house represented a unique combination of soil permeability and aggregate type. Relevant information on house construction, including the size and location of footings and the depth of the aggregate (approximately 10 cm) as a function of position, was monitored and documented.

Soil permeability was measured using a previously described in-situ technique (Garbesi 1988), generally at two locations within the backfill 0.2 m from the basement walls, two locations within the undisturbed soil approximately 3 m from the basement walls, and two locations 1.3 m beneath the aggregate layer.

Experiments were conducted at each house to assess pressure field extension beneath each slab. All visible large cracks and holes in the slab, except the typical gap (wall-slab gap) at the junction of slab and basement walls, were sealed. Temporary SSV systems were installed and operated at each house while measuring the flow rate in the SSV system, the pressure where the SSV pipe penetrated the slab, the pressure at 3 or 4 locations in the backfill area, and the difference between subslab and above-slab pressure at 22 to 35 locations (depending on the house geometry). Holes were drilled through the slab for pressure difference measurements. Short sections of plastic tubing with the upper end capped were inserted through the holes and the junctions of these tubes with the holes

were sealed with duct seal. To measure pressure difference at the location of a specific hole, one side of the differential pressure transducer was manually connected to the upper end of the tube while other tubes remained capped.

SSV flow rates were measured with an orifice plate flow meter (estimated maximum error of 5%). To check these flow rate measurements, a hot wire anemometer and a pitot tube were used to measure air velocity in the SSV pipes. Pressure differences across the orifice plate and between the subslab aggregate and the basement which ranged from a few tenths of a Pa to more than 300 Pa were measured with an electronic pressure transducer (Neotronics EDM with a resolution of 0.1 Pa). The calibration of the electronic pressure transducer was checked by comparison to a micromanometer that uses a micrometer and electronic circuitry to detect fluid level. This manometer has a resolution of approximately 0.5 Pa.

Several experiments were completed, in most houses. Parameters or operating conditions that varied between experiments include: (1) the choice of SSD or SSP; (2) the magnitude of the pressure at the suction or pressurization point (where the SSV pipe penetrates the slab); (3) the presence or absence of a 25 cm radius hemispheric open pit beneath the slab at the suction or pressurization point (called the SSV pit); and (4) open or sealed perimeter wall-floor joint. Table 1 describes the matrix of field tests.

2.2.2 Aggregate Characterization

The aggregates were obtained from local suppliers. The most permeable aggregate type, called 1 1/2" round or 1 3/4" round by the supplier, is approximately equivalent to ASTM Grade No. 4 (ASTM 1984). The medium permeability aggregate, called 3/4" round by the supplier, is approximately equivalent to ASTM Grade No. 67. The lowest permeability aggregate, called 3/8" exposed or #8 pea gravel, is approximately equivalent to ASTM Grade No. 8. Standard information on particle size distribution (i.e., fraction that passes through various size screens) was obtained from the suppliers and is provided in Appendix B.

Samples of the aggregate beneath each slab were shipped to LBL. The relationship between velocity and pressure drop in one sample of each type of aggregate was measured in the laboratory. The basic procedure was to fill a section (25.4 cm by 22.2 cm by 244. cm) of a nearly air-tight box with aggregate, to force air through the aggregate at different rates, and to measure the pressure difference between a location immediately upstream and downstream of the aggregate bed. With the highest permeability aggregate, helium was used in place of air during some tests so that pressure differences could be accurately measured during tests when Darcy flow is expected (i.e., tests with low characteristic Reynolds Numbers as defined in a subsequent section). The laboratory data were analyzed to determine the permeability of the aggregate samples and the value of a another flow-related parameter called the Forchheimer factor (also defined

subsequently). More information on the aggregate samples and the methods and results of laboratory experiments are provided in Appendix B.

2.2.3 Modeling

A new numerical model was developed and used to interpret the experimental data and permit predictions of SSV performance for conditions that were not studied experimentally. Two study houses were modeled in detail and the model was verified to the degree possible by comparison of predictions to the measured field data. The general trends in the model predictions were also compared to the trends from field data (e.g., the effect of sealing the perimeter wall-slab gap on pressure field extension) to further check model performance. The laboratory measurements of the permeability and Forchheimer factor for the aggregates were used as input information for the model. To further investigate SSV performance, a series of parametric computer predictions were completed for a prototypical house with a subslab aggregate layer. The subsequent sections describe the model, the model verification, and the predictions of SSV performance as a function of aggregate type and as a function of variation in other relevant parameters.

Table 1. Matrix of field tests of SSV performance

House No.	No. of Subslab Bays[a]	Soil Permeability Range (m^2)	Backfill Permeability Range (m^2)	Vendor's Aggregate Name	Location(s) of Slab Penetration for SSV	SSV Pit (Y and/or N)	SSD Pressures (Pa)	SSP Pressures (Pa)	Extra Tests With Sealed Wall-Floor Joint (Y or N)
001	3	$4.6\text{-}6.8\times10^{-11}$	$2.8\text{-}10\times10^{-11}$	$\frac{3}{4}$" Round	Center of Central Bay	Y	-125 -375	+125 +375	N
002	2[b]	$1.1\text{-}3.7\times10^{-10}$	$1.9\text{-}3.6\times10^{-10}$	$1\frac{1}{2}$" Round	East Bay, Opening Between Bays	Y and N	-125 -375	+125 +202 +375	N
003	2	$7.5\text{-}9.3\times10^{-11}$	$0.3\text{-}1.1\times10^{-12}$	$\frac{3}{8}$" Exposed	Center of North Bay	Y and N	-125 -375	+125 +375	Y
004[c]	2	BDL	$3.9\text{-}4.6\times10^{-10}$	$1\frac{3}{4}$" Round	Center of West Bay	Y	-125 -375	+125 +375	N
005[d]	2	BDL	BDL - 1.4×10^{-9}	$\frac{3}{4}$" Round	Center of West Bay, Perimeter of West Wall	Y and N	-125 -375	+125 +375	N
006	e	BDL	$8.2\text{-}250\times10^{-12}$	#8 Pea Gravel	Center of East Bay	Y and N	-125 -375	+125 +375	Y

BDL = below detection limit of approximately 10^{-13} m^2.

a Number of subslab regions bounded by footings.

b Footer between bays terminates approximately 0.75 m from one end of slab permitting pressure extension between bays.

c Soil saturated approximately 18 cm below slab.

d Footer between bays terminates approximately 4.3 m from one end of slab permitting pressure extension between bays.

e Three subslab regions; however, interior footings terminate approximately 1 m from perimeter footings permitting pressure extension between bays.

3. Methodology for numerical modeling

3.1. Darcy models

A few sophisticated numerical models have been recently developed (e.g., Loureiro 1990, Mowris 1986, Revzan 1991) to compute the generation and the transport of radon in the soil and its entry into a basement. However, they all assume Darcy's law to determine the soil gas velocity as a function of pressure gradient in the soil.

Loureiro and others use a finite difference method in three dimensional cartesian coordinates to model the house and the soil block. Pressure field and velocity fields are calculated by solving the Laplace equation resulting from the combination of Darcy's law and the continuity equation with the Boussinesq approximation.

Darcy's law states:

$$\vec{V} = -\frac{k}{\mu}\vec{\nabla}p \quad , \tag{1}$$

where

$\vec{V}$ is the gas velocity,

p is the disturbance pressure,

k is the permeability of the porous medium, and

μ is the dynamic viscosity of the fluid.

The continuity equation for incompressible flow can be stated as

$$\vec{\nabla}.\vec{V} = 0 . \tag{2}$$

Substituting for V from Equation (1) in Equation (2) yields

$$\vec{\nabla}.(\frac{k}{\mu}\vec{\nabla}p) = 0 . \tag{3}$$

If locally k and μ are assumed to be constants, the solution can be directly obtained by the solution procedure for Laplace's equation for pressure. This is the basis of all finite difference codes for solving Darcy flow.

Once the velocity and pressure fields are determined, the radon concentration field in the soil and the radon entry rate are computed by separately solving the radon mass balance equation:

$$\vec{\nabla}.(D\ \vec{\nabla}C_{RN}) - \vec{\nabla}.(\vec{V}.C_{RN}) + \varepsilon(S - \lambda_{RN}\ C_{RN}) = 0 \tag{4}$$

where

D is the diffusivity of radon in soil-gas,

C_{RN} is the radon concentration in the soil-gas,

S is the production rate of radon into the soil-gas per cubic meter of bulk soil,

λ_{RN} is the radon decay constant, and

ε is the porosity.

3.2 Non-Darcy models

Darcy's law is a valid description of soil gas (and radon transport) driven by the natural depressurization of a house (about 5 Pa). However it is not a valid description of SSV operation because of the high velocities of soil gas occurring in the subslab aggregate (up to 1.1 m/s). At high velocities, inertial losses, which are proportional to the velocity squared, cannot be neglected. Substantial changes in the algorithms and the solution procedure are necessary to describe non-Darcy flow, compared to the Darcy flow models. Therefore, a new non-Darcy flow simulation model was developed to simulate SSV system performance.

The pressure, P, at any point in the soil can be expressed as

$$P = P_A + p + \rho_0 g z \ , \tag{5}$$

where P_A is the atmospheric pressure, p is the disturbance pressure (i.e., pressure change due to the depressurized basement and/or operation of a SSV system), and $\rho_0 g z$ is the hydrostatic pressure (vertical axis directed down). ρ_0 is the reference volumetric density, g the acceleration due to gravity.

In absence of buoyancy effects, the body force on the fluid is:

$$\vec{F} = \rho_0 \vec{g} \tag{6}$$

The **Darcy-Forchheimer** expression of non-Darcy flow is (Forchheimer 1901):

$$\vec{\nabla} P - \vec{F} = -\frac{\mu}{k}(1 + c\ |\vec{V}|)\vec{V}, \tag{7}$$

where the parameter c is the Forchheimer term.

Substituting Equation (5) and (6) in Equation (7) gives

$$\vec{\nabla} p = -\frac{\mu}{k}(1 + c\ |\vec{V}|)\vec{V}. \tag{8}$$

This equation, in place of Equation (1), must be used to describe the relationship between soil-gas pressure field and velocity field.

The continuity equation (again assuming constant ρ) can still be stated as:

$$\vec{\nabla}.\vec{V} = 0. \tag{9}$$

Equations 8 and 9 constitute the system of equations to be solved. Notice that the two equations can no longer be easily combined, and the methods used for solving the Laplace equation are no longer applicable to solve the system of equations.

Once the soil-gas velocity field is computed, a similarly structured but separate computer program is used to solve Equation (4) for radon advection, diffusion, generation and decay. The solution yields the radon transport through the soil and aggregate and the radon entry rate into the basement.

3.3 The non-Darcy STAR model

The new model called "non-Darcy STAR" (for non-Darcy Simulation of Transport of Air and Radon) is partly inspired by the extension of the Loureiro code by Revzan (1991), and partly by the fluid mechanics model for convective flow by Gadgil (1980). The non-Darcy STAR model simulates all four quadrants of the house and the soil block, thus enabling modeling of non symmetrical, and more realistic, configurations, compared to earlier models which assume some form of spatial symmetry to reduce the size of the computational domain.

Four different solution algorithms were developed and tested for a homogeneous soil block of clean aggregate. All algorithms produced satisfactorily converged solutions, although the convergence speeds varied across algorithms. The algorithm with the best convergence rate was selected for installation in the non-Darcy STAR code.

The solution procedures use a finite difference method, using primitive variables (i.e. fluid pressure and velocity components rather than complex versions of vorticities and stream function) and staggered grids for the pressure and the velocity. We use the Alternate Direction Implicit (ADI) method of iterative solutions. Computations are done with dimensionless variables; see Appendix A for dimensionless transformation. The linearization and discretization of the equations is also described in Appendix A

In a finite difference approach, the equations are solved by discretizing space with a grid, and obtaining the solutions (of the pressure and velocity fields for the soil-gas) on nodes of the grid; the value of the solution at the node represents an average of the solution values over the volume-element surrounding the node. Thus appropriate selection of the grid is an important element of a successful simulation of any particular solution under given boundary conditions.

The grid generation is done by a non-automated or "by-hand" description of the real house. This provides ample accuracy in the solution but also implies less flexibility in changing the grid scheme rapidly to other house geometries.

The model presently incorporates the following three assumptions:

- each material (i.e soil, aggregate) is homogeneous and isotropic;
- the concrete is perfectly impermeable except for cracks; and
- the effect of buoyancy on the soil-gas flow field is negligible.

The geometries of the modeled houses are described in Appendix A.

3.4 Numerical Simulations

The solution procedure employs an iterative approach to convergence. Iterations are stopped when the maximum residual in the pressure field (defined as the fractional change in pressure at any given node from one iteration to the next) falls below 10^{-6}. Computational requirements increase very rapidly with increasing the grid density (i.e. the number of nodes in the computational domain). Therefore, avoiding demands on computational resources must be balanced against retaining an acceptable accuracy of the numerical solutions. For most of the simulations in this study, we selected a grid lay out and a density that provided results for pressure field values within 10% of the values obtained with a much larger (2.5 times the number of nodes) grid density [*].

The simulations have been largely carried out on the Hewlett Packard 9000/730 and SUN 4/280 computers at Lawrence Berkeley Laboratory and on the CRAY 2 supercomputer at Lawrence Livermore National Laboratory. A 3D graphics software package is used for visualization of the pressure field in any given slice of the discretized space (see Figure 1).

[*] The impact of grid density on the simulation results was systematically studied by modeling a 2-dimensional vertical slice of a house and soil block, which allowed us considerable gain in computational speed.

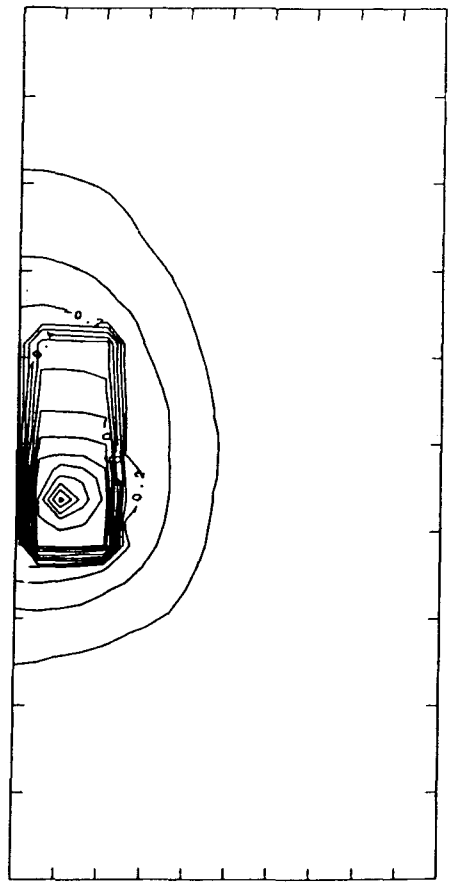

Figure 1 a

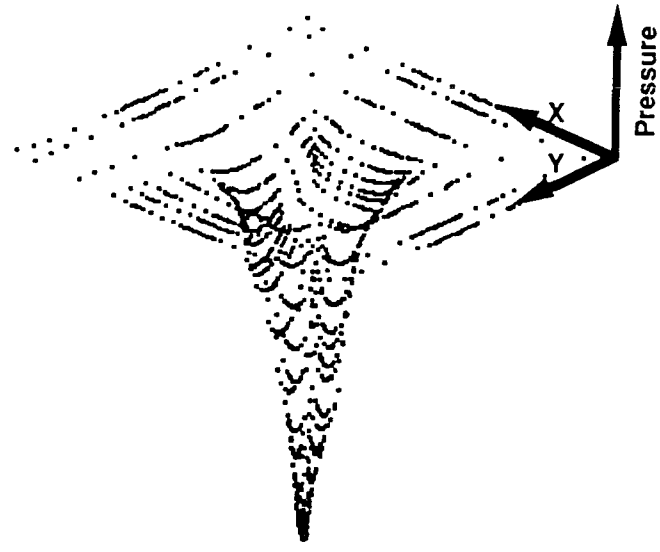

Figure 1 b

(1a) An example of isobars of subslab pressures just beneath the slab generated by SSD operation in a single bay of a basement of an idealized house described in Appendix A. The left edge of the figure is the central footer of the basement, which is also the plane of symmetry for the idealized house.

(1b) An example of a 3-dimensional representation of the pressure field generated by SSD operation in an horizontal slice of computational domain just beneath the footers of a House 002 described in Appendix A.

4. Model Verification.

The numerical model was verified by simulating field experiments performed on houses in the Pacific Northwest, and comparing simulation predictions with experimental results. Verification of the model was considered successful if the predicted subslab pressures at various points in the basement agreed with experimentally measured values, accounting for the uncertainties in the model input data. Four tests at House 002, and two tests at House 003 were simulated. Permeabilities and Forchheimer factors for the subslab aggregate were measured in the laboratory (see Appendix B). The field experiments, described previously, included in-situ measurements of the permeabilities of the soil and backfill material. The applied pressure at the SSV pit was also measured during the tests. The simulations assumed no pressure difference between the basement and the outside during the tests because the basements were unheated and open to the outside during field experiments. These values, and the geometrical description of the houses were used as inputs to the simulations. The cracks between the basement slab and the wall/footers were assumed to be of uniform thickness at all wall/footer/slab joints, (i.e at the basement periphery and around the middle footer). The input parameter values for these simulations are shown in Tables 2 and 3.

The average or effective thickness of the cracks cannot be measured experimentally in a reliable manner. We show (Figure 2) the predictions from two simulations, one with perfectly sealed cracks and another with wide (3 mm) L-shaped cracks. The predictions bracket the experimental data for subslab and backfill pressures at all the points. Furthermore, we also show in Figure 2 that predictions, made assuming a 1.1 mm wide L-shaped crack all along the slab-footer joint, agree well with experimental data for pressures collected at 22 different subslab locations, and 3 points in the backfill region. The positions of the measurement (and prediction) points for subslab and backfill pressures are shown in Figure 3 on a schematic floor plan of House 002. The measured flow during field experiments and the predicted flow in the SSV pipe also agree well (within 10%). Data in Figure 2 are for two tests, which respectively have SSP and SSD operation with a pressure (or suction) of 125 Pa applied at the SSV pit (shown as S-1 in Figure 3).

Two additional tests at House 002 (SSD and SSP operation using 200 Pa), were then simulated without changing any of the other input parameters in the model. The predictions again agree well with the experimental pressure data at the measurements points (comparison not shown for brevity).

A similar verification exercise was undertaken using soil, aggregate and configuration geometry of House 003, and field experiment data from two tests (SSD and SSP operation at 125 Pa). Figure 4 shows the experimental pressure measurements at 27 subslab points bracketed by simulation predictions assuming no cracks and wide (3 mm) L-shaped cracks. The measured pressures are reasonably well matched by predictions assuming a 0.75 mm L-shaped crack at all slab-footer joints (the locations of the measurement points are shown in Figure 5).

It should be noted that while the sets of input parameters shown in Tables 2 and 3 are certainly realistic and consistent with measurement data on soil and aggregate permeability values, there exist enough uncertainties in the experimental data on these values that the input parameter set is not unique. For example, choice of a somewhat higher permeability for the soil and a narrower crack thickness leads to similar predictions from the simulations. We can also obtain agreement with experimental data assuming non-uniform crack thickness along the slab footer joints, and inhomogeneous soil permeability. However, in the absence of experimental evidence in support of such artifacts in the input data to the simulations, the excellent agreement of resulting simulation predictions with experimental measurements becomes a mere curiosity. The agreement between simulation predictions and field experimental data shown in Figures 2 and 4 is therefore considered adequate under these circumstances.

Table 2: Inputs for modeling of House 002.

Aggregate	Soil	Backfill	Crack
$k = 3.0\text{x}10^{-7}\ m^2$ $c = 20\ s/m$	$k = 10^{-10}\ m^2$ $c = 0\ s/m$	$k = 10^{-10}\ m^2$ $c = 0\ s/m$	1.1 mm L-shaped

Table 3: Inputs for modeling of House 003.

Aggregate	Soil	Backfill	Crack
$k = 2.0\text{x}10^{-8}\ m^2$ $c = 6\ s/m$	$k = 9.0\text{x}10^{-11}\ m^2$ $c = 0\ s/m$	$k = 9.0\text{x}10^{-11}\ m^2$ $c = 0\ s/m$	0.75 mm L-shaped

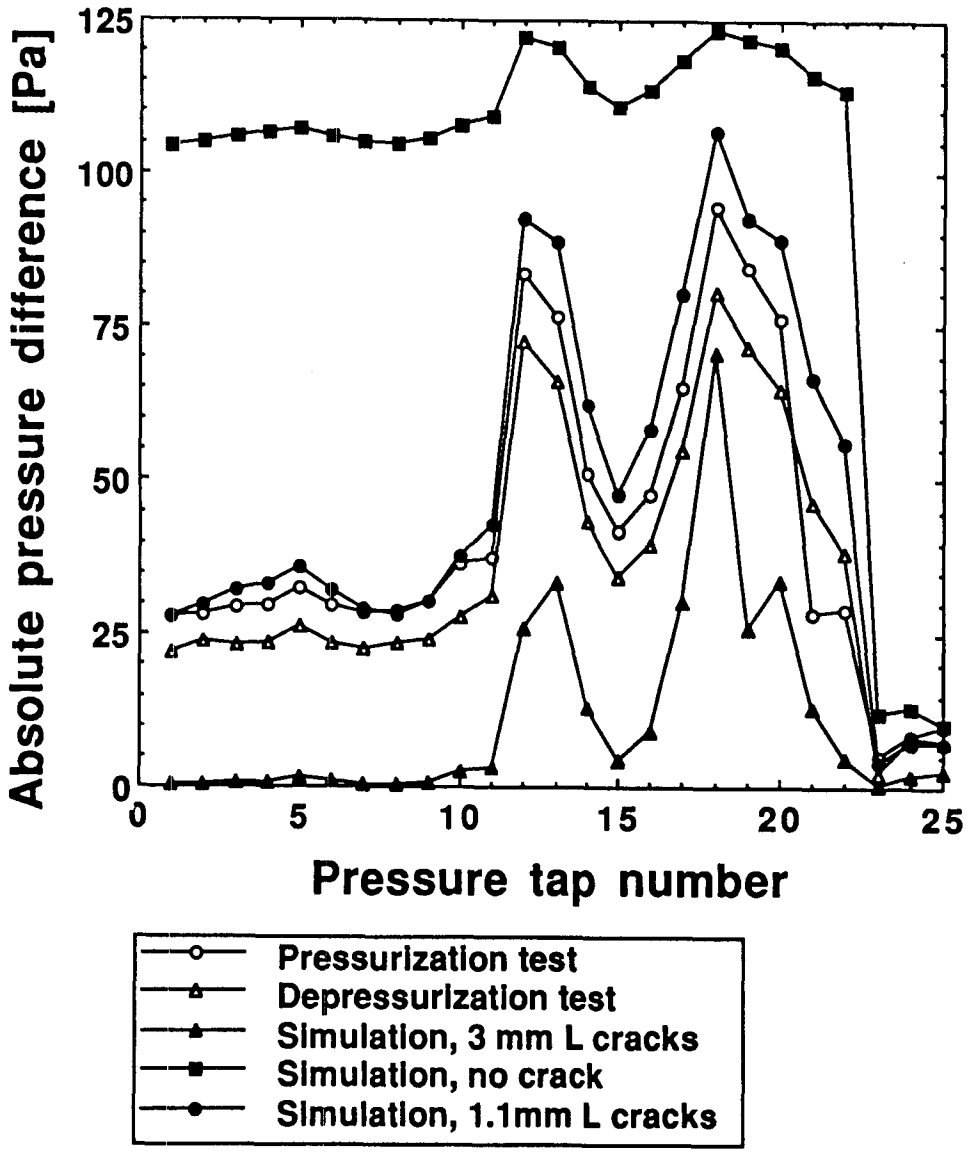

Figure 2 .
Comparison of field measurements and numerical predictions of subslab pressures at various points in House 002.

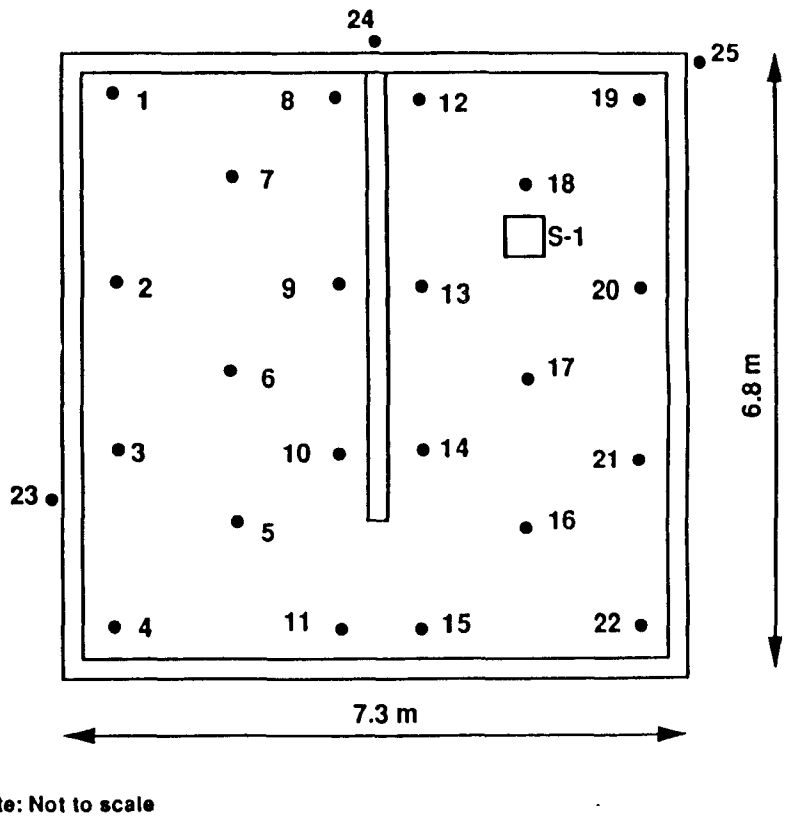

Figure 3 .
Subslab pressure tap locations and identification numbers in the basement slab of House 002. Perimeter and interior footing are shown.

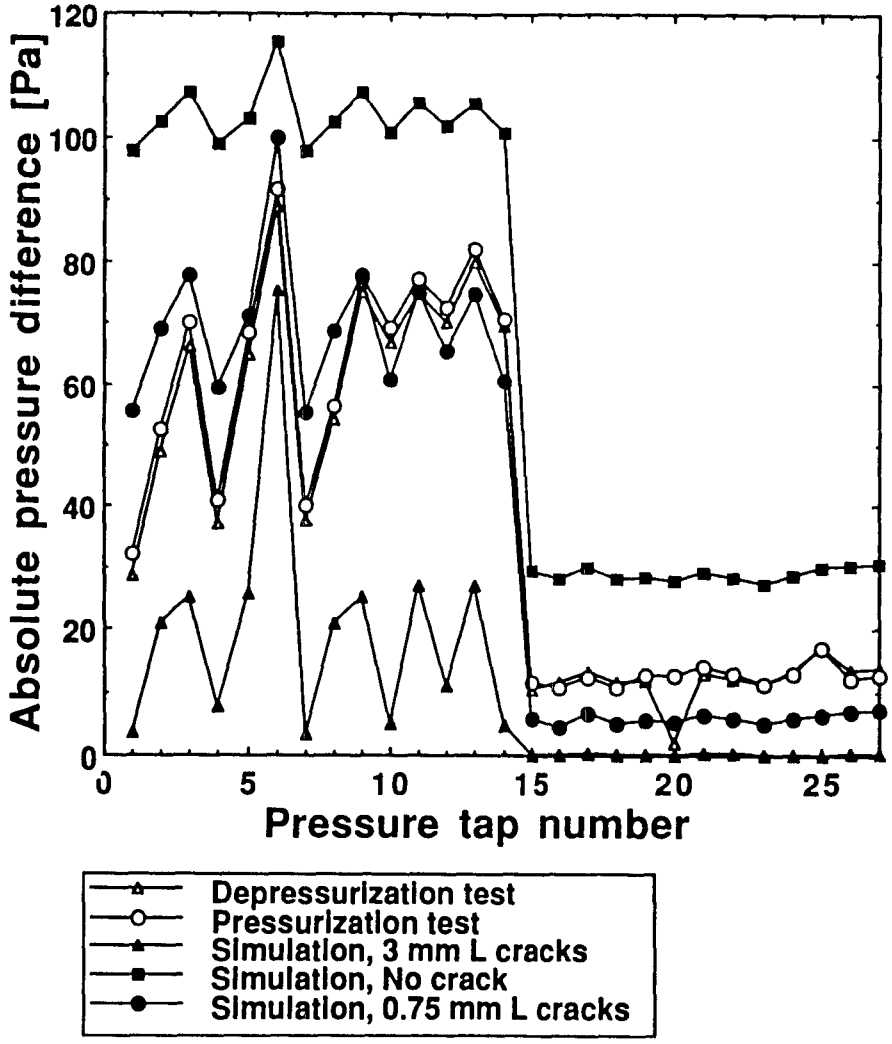

Figure 4 .
Comparison of field measurements and numerical predictions of subslab pressures at various points in House 003.

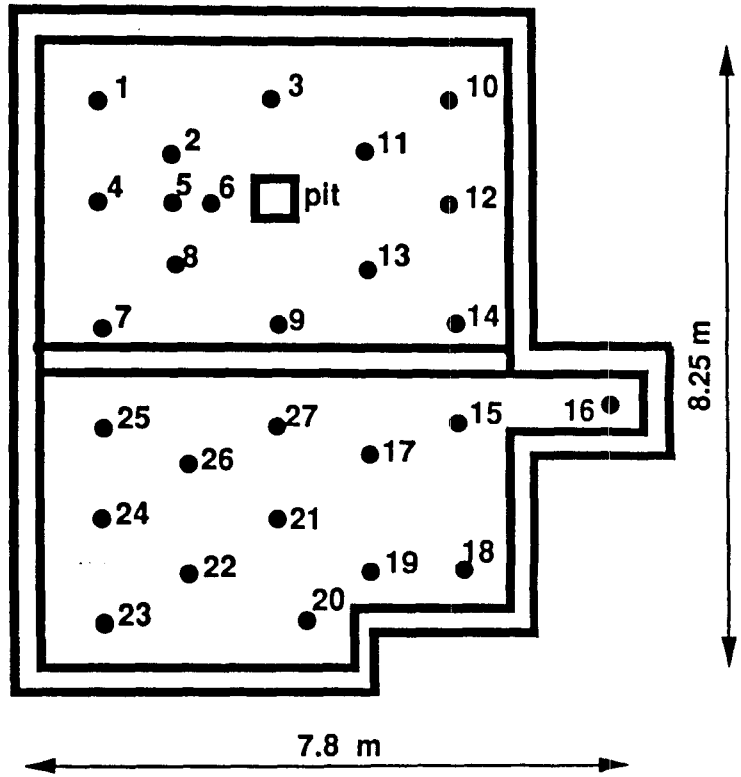

Note: not to scale

Figure 5 .
Subslab pressure tap locations and identification numbers in the basement slab of House 003. Perimeter and interior footing are shown.

5. Trends in the Field Data and Simulation Predictions

Based on field data, this section describes the dependence of subslab pressure fields on selected features of the SSV system and substructure and also on the ratio of aggregate to soil permeability. In several cases, the same dependence is illustrated based on numerical predictions. The qualitative correspondence of experimental results and numerical predictions serves as an additional confirmation of model performance.

5.1 Effect of a pit in the subslab aggregate at SSV installation point.

Field data demonstrate that excavating a small (25 cm radius) pit at the point of SSV system penetration through the slab substantially improves the extension of the pressure field in the subslab region (see Figure 6, where measured pressure differences at test holes have been normalized by depressurization at the pit). This beneficial effect of a SSV pit has also been demonstrated in prior research (Furman and Hintenlang 1990). In the absence of a pit, the extension of the pressure field can be expected to be affected by the specific details of the arrangement of the aggregate particles immediately adjacent to the hole in the slab. In addition, openings in the surface of the aggregate may be obstructed by residual dust or sand produced from the drilling of the hole in the slab or pores in the aggregate may be plugged with concrete. Since SSV system performance is more reliable and effective when the SSV systems are installed with a pit excavated in the subslab aggregate, all further investigations on the effectiveness of SSV system performance assume that the SSV system installations have already incorporated this basic and inexpensive measure; we explore effects of other factors on SSV performance.

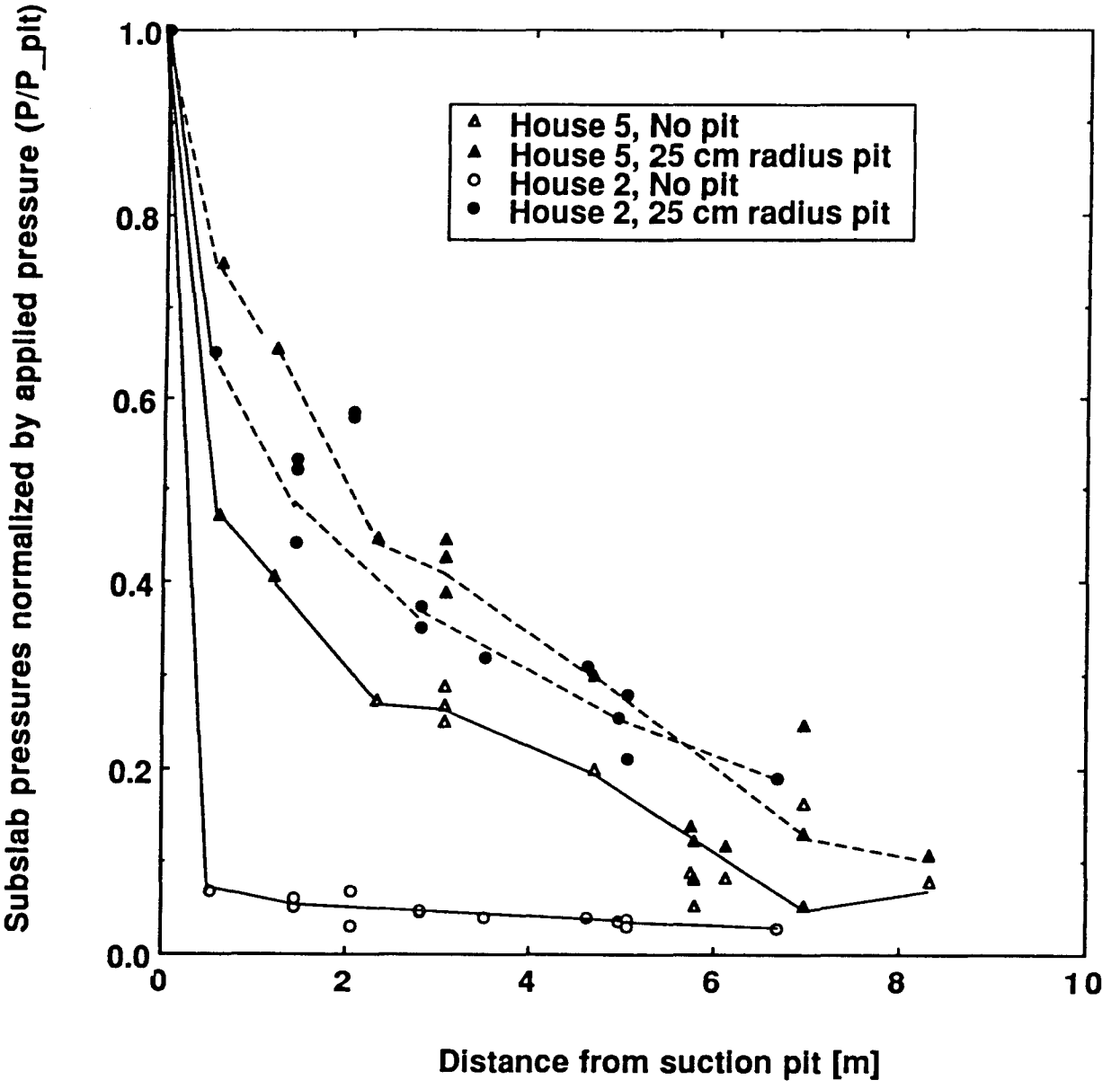

Figure 6

Effect of pit in the subslab gravel at the point of SSV installation. Subslab pressure field extension for houses 002 and 005 improved substantially after a 25 cm radius pit was excavated in the subslab gravel at the point of SSV installation.

5.2 Effect of the magnitude of applied pressure.

Both the experimental data (Figure 7a) and numerical predictions (Figure 7b) indicate that the normalized values of the subslab pressure field (range 0-1) at all subslab points are larger (more negative) for smaller depressurizations at the suction pit, P_pit. The trend is due to non-Darcy flow of soil-gas during SSV operation. At larger values of P_pit, soil-gas velocities in the aggregate increase and, as noted previously, inertial losses increase in proportion to the velocity squared. Thus a larger pressure gradient is required to maintain a given soil gas velocity than indicated by the Darcy law. In practical terms, the pressurization or depressurization in the aggregate increases sub-linearly with increasing pressure (or suction) applied at the pit.

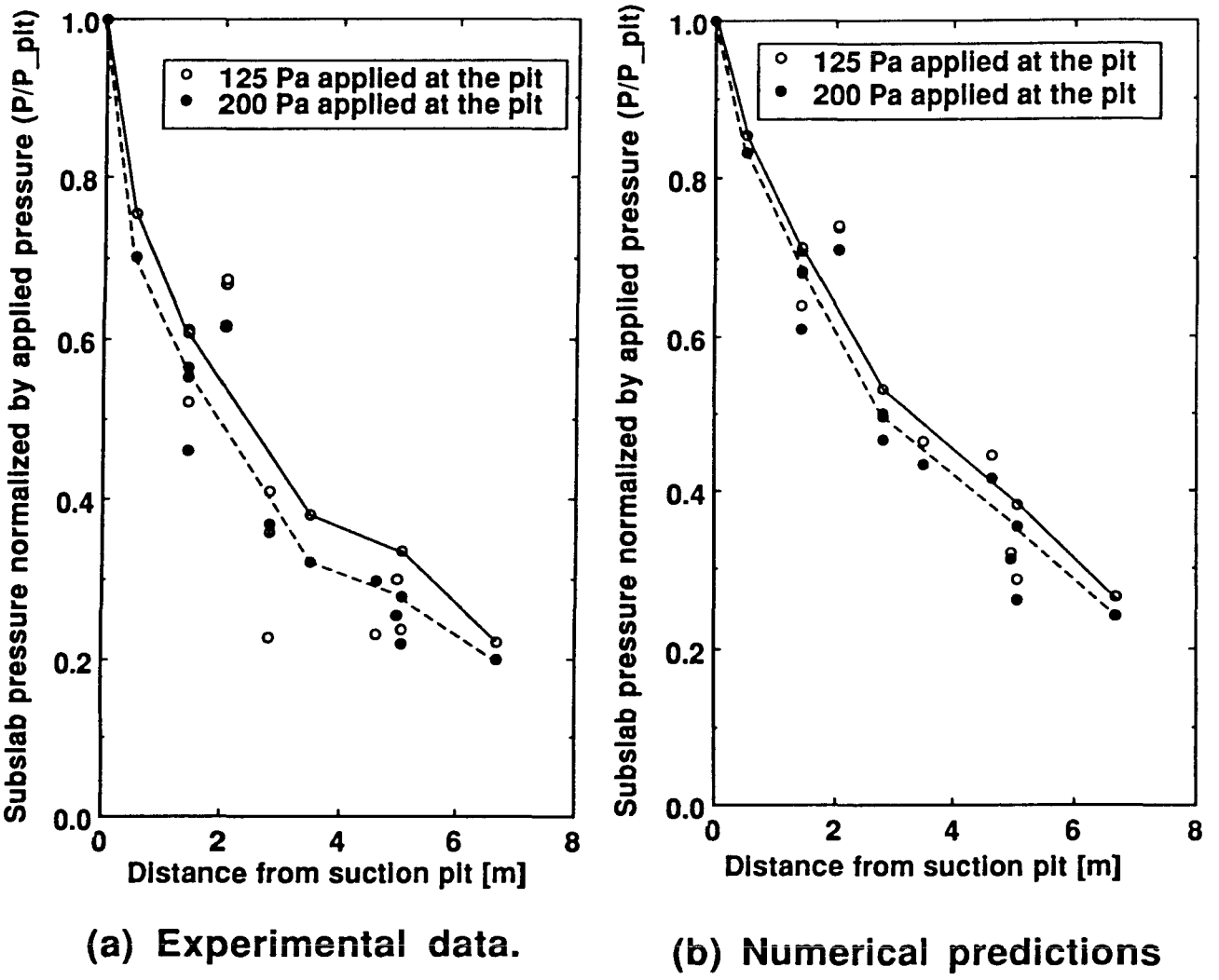

Figure 7 .

Effect of applied pressure (P_pit) is manifested as non-Darcy flow lowers the normalized subslab pressure at all points (Fig. 7a). The same effect is demonstrated in simulation predictions (Fig. 7b). Dashed and continuous lines show trends in data points for different applied pressures. The lines on these figures connect data from a subset of the measurement locations and are intended for visual guidance only.

5.3 Effect of the ratio of aggregate permeability to soil permeability

From analogy with electrical circuit theory, it is anticipated that the subslab aggregate will yield excellent pressure field extension (i.e. act as a pressure manifold), if the ratio of aggregate permeability to soil permeability is large. One also expects that as this ratio decreases towards unity, the pressure field extension in the subslab region would get progressively poorer as the resistance to soil-gas flow through the aggregate is no longer significantly less than the resistance to flow through the soil beneath the aggregate.

Experimentally observed confirmation of this effect is shown in Figure 8, using data from three different houses. Since each house has a somewhat different geometry, these data are not directly intercomparable. Simulations with non-Darcy STAR for a fixed house geometry and different combinations of soil and aggregate permeabilities, discussed in Section 5, also indicate that the ratio of aggregate permeability to soil permeability has a critical impact on pressure field extension.

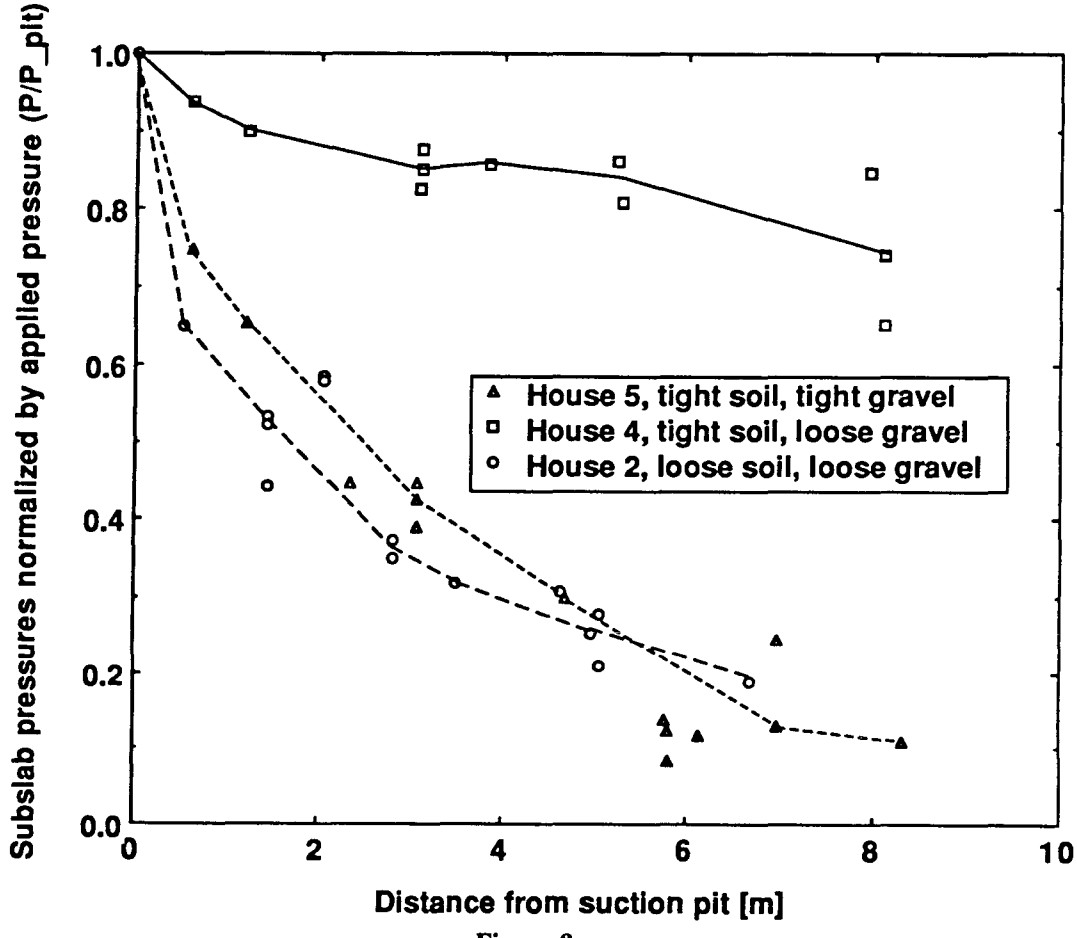

Figure 8 .

Measured subslab pressure field extension data from three houses with different combinations of soil and gravel permeability. The terms "loose" and "tight" refer to high permeability and low permeability, respectively. Theory and simulations predict that subslab pressure field extension should be excellent when the ratio of gravel to soil permeability is large; an effect observed in the experimental data shown. Since each of the three houses has a different geometry, individual data points should not be directly compared to draw conclusions. The lines on this figure are intended for visual guidance only.

5.4 Effect of the sealing of the cracks.

After a first set of field experiments on subslab pressure field extension in House 006, the cracks at the slab-footer joints were carefully sealed, followed by a second set of experiments. Experimental data, Figure 9a, demonstrate the substantial improvement in the subslab pressure field extension following the sealing of the cracks. Simulations with the non-Darcy STAR model using the House 002 geometry (note the different house number) also show a similar dramatic improvement in predicted subslab pressure field extension following sealing of all slab-footer cracks (see Figure 9b).

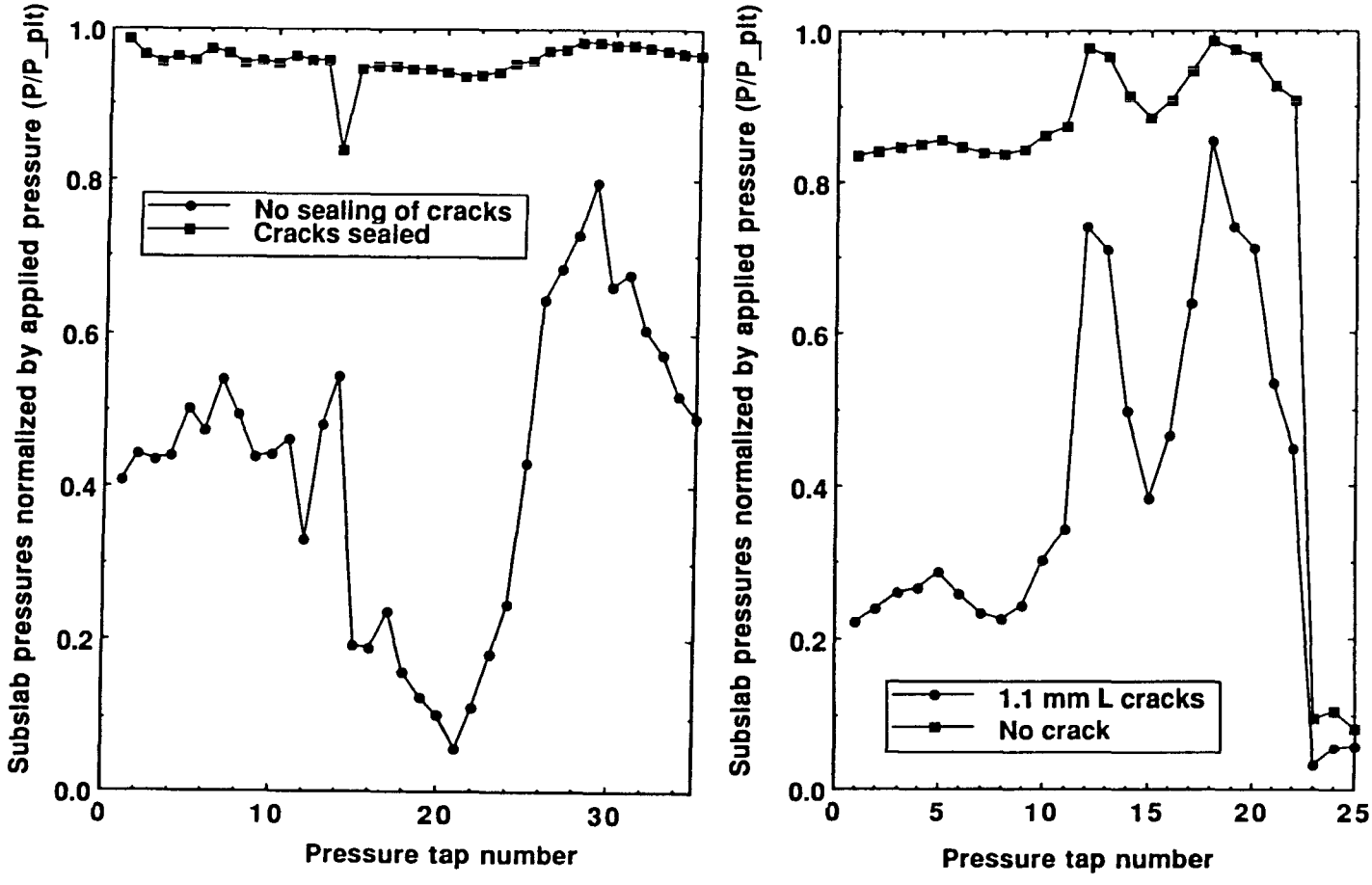

(a) House 006, Experimental Data. **(b) House 002, Numerical Predictions.**

Figure 9.

Sealing of slab-footer cracks leads to substantial improvement in the subslab pressure field extension as demonstrated by field experiment data for House 006 (Fig. 9a) and numerical predictions for House 002 (Fig. 9b).

5.5. Discussion of Trends in Field Data and Numerical Predictions.

Three major conclusion can be deduced from the trends in field data and numerical predictions. The conclusions all relate to good extension of the pressure field in the entire region beneath the basement slab. If such extension is successful, then it may prevent the entry of radon bearing soil gas into the basement. For SSD, with sufficient pressure field extension soil gas will not enter the depressurized basement through the cracks. For SSP, we expect that the air flow entering the basement through the cracks will have a low radon concentration, as this air should be primarily fresh air blown in from the pit. However, if the extension is incomplete, radon will be advectively transported into depressurized portions of the subslab aggregate layer and then be carried into the basement. The three conclusions can be summarized as follows:

1) Pressure field extension in the sub-slab region is very substantially improved if the SSV system is operated with a pit (radius about 25 cm) excavated in the aggregate and soil, at the point where the suction pipe penetrates the basement slab.

2) Sealing all the visible cracks in the slab (including those that appear at the wall-slab joints owing to slab shrinkage) to the extent possible, leads to a significantly improved performance of SSV system as measured by sub-slab pressure field extension.

3) When aggregate is much more permeable than the soil (and cracks and openings in the basement floor are sealed), the aggregate acts as a depressurized manifold with respect to the basement during SSD operation (i.e. there is improved subslab pressure field extension). On the other hand, when the ratio of aggregate permeability to soil permeability is low, (specifically, it is smaller than about two orders of magnitude), considerable pressure drops can be expected within the aggregate bed.

6. Results from Simulation Studies

6.1 Simulation Description

The non-Darcy STAR model was used with an idealized house geometry in a series of parametric studies to address the primary objective of this research effort: to determine the influence of sub-slab aggregate characteristics on the performance of SSV systems.

The idealized house geometry has a simple rectangular plan. It has a full basement and an attached garage at the ground level on one side. The sub-slab area is divided into two symmetric bays by a central footer, each bay having its own SSV system. The size of each bay is 3.5 m by 7 m. A 1 mm thick L-shaped crack is present along the perimeter of each bay. The geometry of the idealized house is described in greater detail in Appendix A.

The backfill region surrounding the house has the same permeability as the soil. This assumption is consistent with the field data from houses surrounded by soil with a permeability greater than $10^{-12}\,m^2$. The basement is assumed to be depressurized to -10 Pa relative to the atmosphere (-10 Pa represents an approximate upper limit to the basement depressurization under actual conditions). Soil-gas and radon entry into the idealized house were studied using the simulation model for three different soil permeabilities ($10^{-11}m^2$, $10^{-10}m^2$, and $10^{-9}m^2$). A soil permeability of $10^{-9}\,m^2$ is unusually high, even for Pacific Northwest soils which sometimes have a permeability greater than $10^{-10}\,m^2$. However our simulations are based on homogeneous soil. We suspect that heterogeneous soils with an average permeability of $10^{-10}\,m^2$ could contain high-permeability pathways and affect SSV system performance similarly to higher permeability (e.g., $10^{-9}\,m^2$) soils. We also used three different aggregate types in our simulations with permeabilities and Forchheimer terms corresponding to values measured for the three different aggregate types used in the field experiments (see Table B2, Appendix B). The performance of both Sub-Slab Depressurization (SSD) systems and Sub-Slab Pressurization (SSP) systems was investigated.

6.2 Influence of Aggregate and Soil Permeabilities on SSV Performances

6.2.1 Sub-Slab Depressurization (SSD) System

Table 4 provides results of parametric simulations of SSD performance. Each row of the table corresponds to a different combination of soil permeability, aggregate permeability, and depressurization at the SSV pit.

Based on these simulations, there is only one instance of failure of SSD as indicated by a non-zero soil-gas entry rate. This failure occurs for a low aggregate permeability, a high soil permeability, and the lower of the two depressurizations at the SSV pit (-60 Pa).

In the fifth column of Table 4, we provide values of the parameter "Pmax (30 cm)". This parameter is the algebraically largest subslab pressure (referenced to outdoor pressure) at a location thirty centimeters inside of a wall. To prevent radon entry, this pressure should be smaller (more negative) than the basement pressure (referenced to outside pressure) which is -10 Pa for the simulations. An increase in aggregate permeability clearly leads to better (more negative) values of Pmax (30 cm).

The difference between the assumed basement pressure of -10 Pa and Pmax (30 cm) is called the excess depressurization. The excess depressurization is the amount of depressurization beyond that required to prevent radon entry. A larger excess depressurization may be considered as a larger safety factor and therefore is desirable. This parameter is provided in the sixth column of Table 4. With a -60 Pa SSD pit pressure, use of the lowest permeability aggregate results in one predicted instance of SSD system failure and only a small excess depressurization ($\leq$6 Pa) in other cases. Switching to the medium or high permeability aggregate leads to excess depressurizations of 9 to 29 Pa. Maintaining a high (250 Pa) depressurization at the SSD pit also results in excess depressurizations of 12 to 36 Pa with the lowest permeability aggregate; however a larger fan and SSV flow rate are required.

The seventh column of Table 4 lists values for the SSD Pressure Extension Ratio (SSD-PER) which equals Pmax (30 cm) divided by the depressurization at the SSV pit. This parameter is a direct measure of the extent of pressure field extension under the slab and higher values indicate improved extension. SSD-PER is plotted versus aggregate permeability in Figure 10. We see that pressure field extension improves substantially with increased aggregate permeability. For example, switching from the lowest permeability aggregate to the medium permeability aggregate increases the SSD-PER by approximately a factor of two and a switch from the medium to highest permeability aggregate increases the SSD-PER by about another factor of 1.4 . SSD-PER also improves modestly when soil permeability decreases from $10^{-9}\,m^2$ to $10^{-10}\,m^2$. A further decrease in soil permeability to $10^{-11}\,m^2$ has little effect on SSD-PER for the cases examined.

Ideally, the subslab depressurization will remain sufficient in magnitude to prevent radon entry even if the depressurization at the pit (P_pit) is decreased to a low value. Figure 11 provides plots of Pmax (30 cm) for various combinations of aggregate and soil permeability. The slope on the curves depend primarily on the aggregate permeability. However, the value of P_pit required to prevent radon entry depends more directly on the ratio of aggregate to soil permeability ($\frac{K_g}{K_s}$). With ($\frac{K_g}{K_s}$) equal to 20 and an aggregate permeability of $2.\text{x}10^{-8}\,m^2$, the depressurization at the pit must exceed 65 Pa to prevent

radon entry into the idealized house. In contrast, with $(\frac{K_g}{K_s})$ equal to 1000, a depressurization at the pit slightly greater than 12 Pa will prevent radon entry. Consequently, with a high ratio of aggregate permeability to soil permeability, a less powerful SSV fan is required for radon control. Alternately, for a given value of P_pit, the margin of safety (depressurization in excess of that required to prevent radon entry) increases with increased $(\frac{K_g}{K_s})$.

The eighth and ninth columns of Table 4 contain the predicted SSV flow rates. With the very high soil permeability of $10^{-9}\,m^2$, and a SSV pit pressure of -250 Pa, two of the flow rates exceed 0.07 m^3/s (150 cfm). Many commonly used SSV fans cannot produce such a high flow rate, instead a lower pit pressure would normally be accepted.

The tenth column lists the rate at which basement air is drawn into the soil through the cracks by the SSV system. Unless the soil is unusually permeable ($10^{-9}\,m^2$), we predict that most of the air exhausted by the SSV system comes from the basement. Consequently, the SSV system will increase the ventilation rate of the house. These predictions are consistent with the results of tracer gas tests in actual houses (Turk et al. 1989). Because SSV system operation increases ventilation rates, heating and air conditioning loads will be reduced by selecting a high permeability aggregate in contrast to maintaining a large depressurization at the pit. To indicate the approximate magnitude of ventilation rate increases, we divide the basement-to-soil flow rate by the indoor volume (assuming the house has one above-grade floor) and convert this number to an effective air exchange rate in air changes per hour. The resulting effective air exchange rate (column 11) ranges from 0.13 to 2.3 air changes per hour. A typical residential ventilation rate in Pacific Northwest houses is 0.4 air changes per hour (Palmiter, 1989), consequently a SSD system can cause large increases in the ventilation rate.

The final column of Table 4 provides the mass defect which is the percentage error in the total soil-gas/air mass balance. The balance is excellent in all cases, which indicates that a converged solution has been reached.

To summarize our major findings, the excess depressurization, and the pressure field extension improve substantially with increasing aggregate permeability and also as soil permeability decreases from $10^{-9}\,m^2$ to $10^{-10}\,m^2$. In addition, a large ratio of aggregate permeability to soil permeability reduces the need for large depressurizations at the SSV pit and associated high SSV flow rates.

Table 4: Model inputs and results of parametric study of SSD system performance in the idealized house.

Soil perm. [m^2]	Aggregate perm. [m^2]	Perm ratio	Suction at pit [Pa]	Pmax (30 cm) [Pa]	(1)Excess Depress. [Pa]	(2)SSD-PER	SSV Fan flow		Soil gas Entry [m^3/s]	Basement-to -soil flow		Mass defect [%]
							[m^3/s]	[cfm]		[m^3/s]	(3)ACH	
10^{-9}	$2.0x10^{-8}$	20	-60	-9.6	-0.4	0.16	0.015	32	$1.6x10^{-5}$	$4.5x10^{-3}$	0.13	0.02
10^{-9}	10^{-7}	100	-60	-19.	9.	0.31	0.029	61	0.	0.013	0.38	0.08
10^{-9}	$3.0x10^{-7}$	300	-60	-28.	18	0.46	0.04	85	0.	0.02	0.59	0.2
10^{-10}	$2.0x10^{-8}$	200	-60	-15.	5	0.25	0.008	17	0.	$8.2x10^{-3}$	0.24	0.04
10^{-10}	10^{-7}	1000	-60	-28.	18	0.46	0.02	42	0.	0.018	0.53	0.1
10^{-10}	$3.0x10^{-7}$	3000	-60	-38.	28	0.63	0.028	59	0.	0.025	0.73	0.4
10^{-11}	$2.0x10^{-8}$	2000	-60	-16.	6	0.27	0.009	19	0.	0.009	0.26	0.04
10^{-11}	10^{-7}	10000	-60	-29.	19.	0.49	0.019	40	0.	0.019	0.55	0.2
10^{-11}	$3.0x10^{-7}$	30000	-60	-39.	29	0.66	0.026	55	0.	0.026	0.76	0.5
0.	$2.0x10^{-8}$	∞	-60	-16.	6	0.27	0.009	19	0.	0.009	0.26	0.04
0.	$1.0x10^{-7}$	∞	-60	-29.	19	0.49	0.018	38	0.	0.018	0.53	0.2
0.	$3.0x10^{-7}$	∞	-60	-39.	29	0.66	0.026	55	0.	0.026	0.76	0.4
10^{-9}	$2.0x10^{-8}$	20	-250	-22.	12	0.09	0.054	110	0.	0.019	0.55	0.02
10^{-9}	10^{-7}	100	-250	-48.	38	0.19	0.088	190	0.	0.039	1.14	0.08
10^{-9}	$3.0x10^{-7}$	300	-250	-72.	62	0.29	0.120	250	0.	0.057	1.67	0.02
10^{-10}	$2.0x10^{-8}$	200	-250	-40.	30	0.16	0.034	72	0.	0.029	0.85	0.03
10^{-10}	10^{-7}	1000	-250	-87	77	0.34	0.062	130	0.	0.055	1.62	0.02
10^{-10}	$3.0x10^{-7}$	3000	-250	-120.	110.	0.48	0.084	180	0.	0.076	2.23	0.5
0.	$2.0x10^{-8}$	∞	-250	-46.	36.	0.18	0.031	66	0.	0.031	0.91	0.03
0.	10^{-7}	∞	-250	-97.	87.	0.39	0.058	122	0.	0.058	1.70	0.6
0.	$3.0x10^{-7}$	∞	-250	-130	120	0.51	0.08	170	0.	0.079	2.32	0.6

(1) Excess Depress. = Excess Depressurization = Basement Pressure (-10 Pa) minus Pmax (30 cm).

(2) SSD-PER = SSD Pressure Extension Ratio = Pmax (30 cm) / suction at pit.

(3) Equivalent air changes per hour of house assuming a total height between basement floor and house ceiling of 5 m.

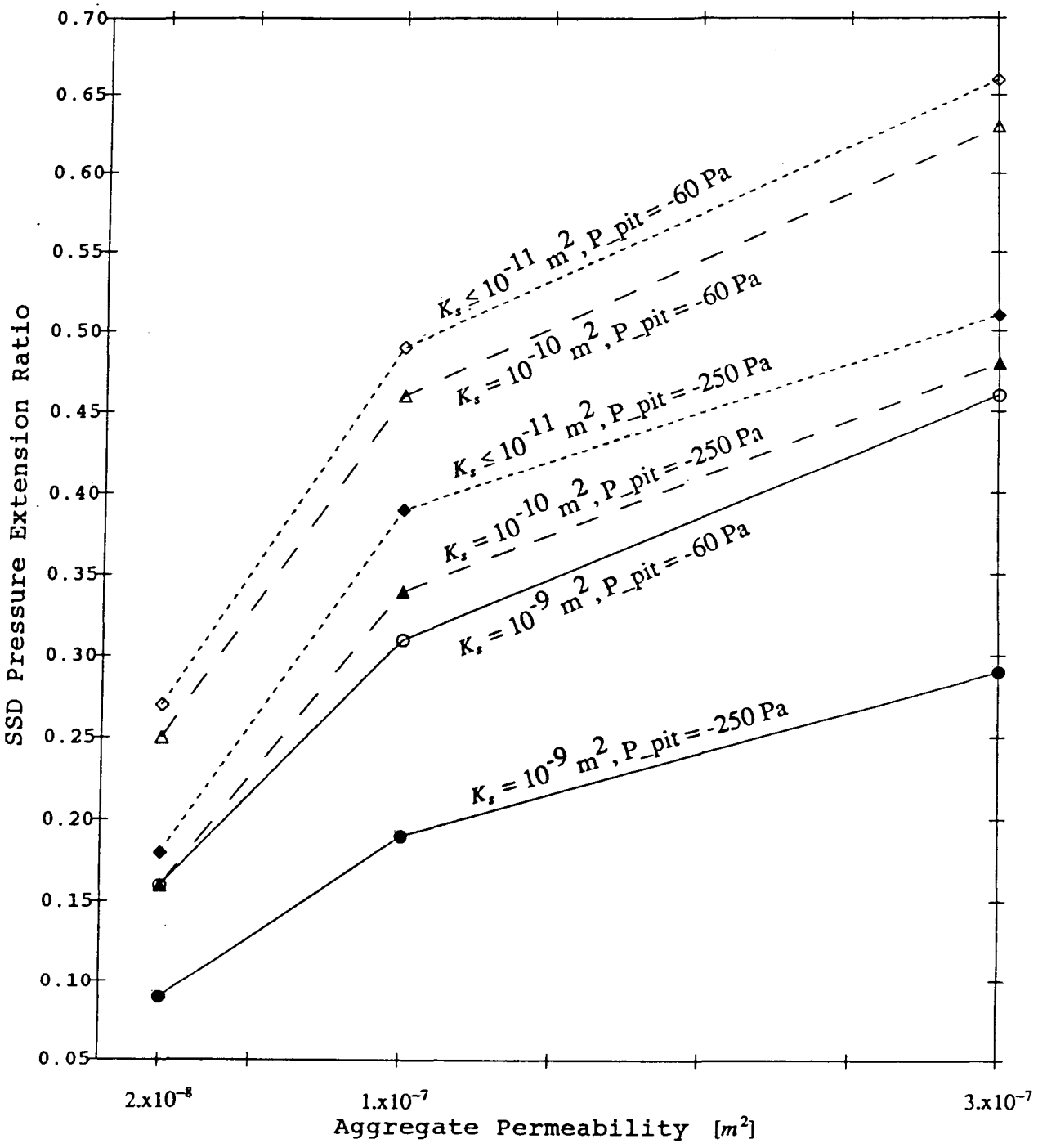

Figure 10.

SSD Pressure extension Ratio versus aggregate permeability for the idealized house.

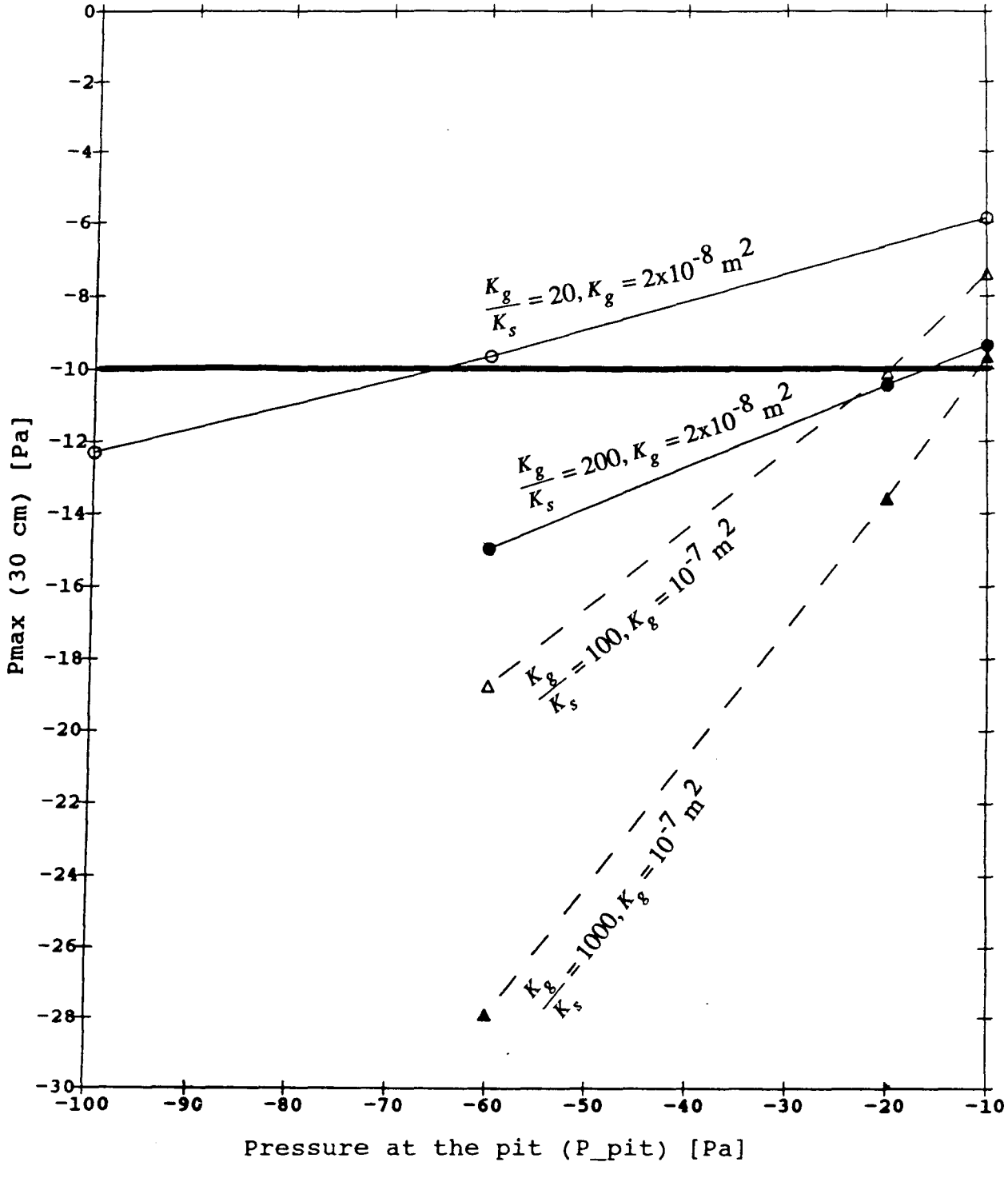

Figure 11.

Depressurization beneath the basement slab of the idealized house as indicated by Pmax (30 cm) versus pressure at the SSV pit. The assumed pressure in the basement is -10 Pa. Soil-gas entry occurs for points above the line of Pmax (30 cm) equal to -10 Pa.

6.2.2 Sub-Slab Pressurization (SSP) system

A similar series of parametric simulations, using the idealized house, was undertaken for SSP system performance. The simulations clearly brought out three significant factors that characterize successful reduction of radon entry rates using SSP.

- Good extension of the subslab pressure field correlates with good SSP performance.
- A large flow resistance of the slab-footer cracks relative to the flow resistance of the sub-slab aggregate improves SSP performance.
- A large value for the soil permeability under the subslab aggregate reduces radon diffusion into the air that flows beneath the slab and enters the basement through the perimeter crack.

While the first factor may be self evident since pressure field extension due to SSP and SSD are analogous, the second and the third factors deserve some explanation. The second factor, a high crack resistance relative to aggregate resistance, reduces convective entry of radon bearing soil-gas into the subslab aggregate layer. As a result of positive pressure at the SSP system installation point (at the pit), and a negative pressure in the basement communicated through slab-footer cracks to the subslab aggregate, there is a plane of zero pressure in the subslab aggregate (or possibly in the crack). On the SSV pit-side of this plane the pressure is positive, and on the crack side it is negative. Soil-gas is drawn into negative pressure region of the subslab aggregate and enters the basement through the cracks. Even if the soil were perfectly impermeable or a perfect membrane was installed beneath the aggregate (see Table 5), the plane of zero pressure is more than 30 cm away from the wall in the case of a tight (i.e low permeability, $2.0\ 10^{-8}\ m^2$) aggregate and a 1 mm thick L-shaped crack. In this case, soil-gas entry occurs. Increasing the aggregate permeability or decreasing the crack size reduces the size of the depressurized region that draws soil-gas into the aggregate layer.

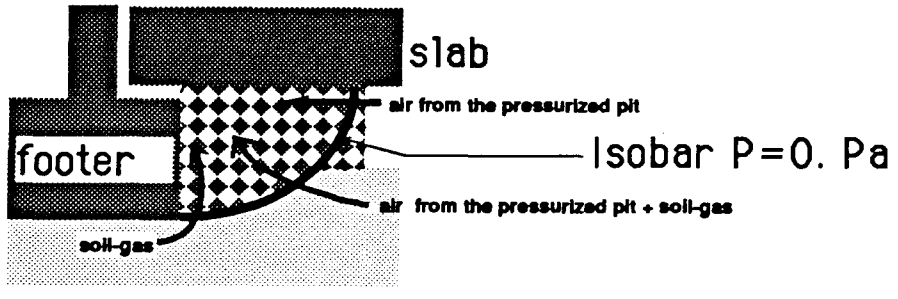

The third factor, a high soil permeability, reduces diffusive entry of radon into the subslab aggregate layer. When the soil is highly permeable, air flows from the subslab aggregate layer into the soil at large enough velocities that diffusion of radon upstream into the aggregate becomes impossible. However, when the soil has low permeability, air velocities from the aggregate into the soil are extremely small, and diffusion of radon

upstream into the aggregate can become the main mechanism of radon entry into the subslab aggregate and from there into the basement.

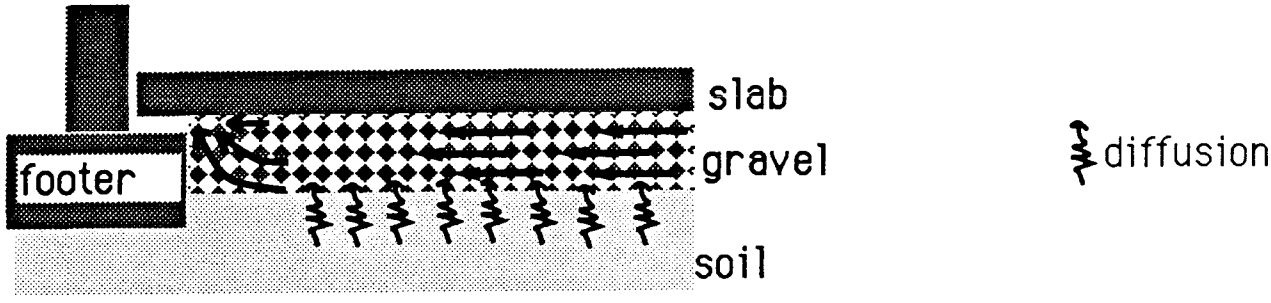

Table 5: Results of simulations of SSP system performance with a perfect membrane under the aggregate layer.			
Kg $[m^2]$	Pmin (30 cm) [Pa]	gas entry $[m^3/s]$	Mass defect [%]
2.0×10^{-8}	-1.1	0.012	$2. \times 10^{-6}$

Table 6 provides the results of the parametric simulation of SSP system operation. The parameters in this table are similar to those in Table 4. Pmin (30 cm) is the minimum subslab pressure (relative to outdoors) at a location thirty centimeters inside of a wall. For effective SSP system operation, Pmin (30 cm) must be greater than zero; however, SSP system performance is not fully characterized by the subslab pressure field as indicated in the subsequent discussion.

We provide the predicted radon entry rate in column 9 of Table 6. To indicate the potential significance of the predicted radon entry rate during SSP operation, we also include an indoor radon concentration (C_{indoor}) in the table based solely on the predicted rate of radon entry through cracks in the slabs. (Diffusive radon entry through the concrete, radon released from water, and radon entry via outdoor air flow into the house are neglected). C_{indoor} is computed as follows

$$C_{indoor} = \frac{(3600)\, S_{Rn}\, C_{\infty} \times 10^{-6}}{V \sqrt{0.4^2 + ((F/V)\,(3600))^2}} \qquad (10)$$

where

S_{Rn} is the normalized radon entry rate in cm^3/s from column 10 of Table 6 ,

C_{∞} is the assumed soil gas radon concentration in deep soil,

F is the soil-to-basement flow (column 8),

0.4 is a typical air exchange rate in air changes per hour for Pacific Northwest houses (Palmiter 1989),

V is the indoor (basement plus house) volume, more precisely V is the product of the basement floor area (Appendix A) and an assumed total height between basement floor and house ceiling of 5 meters, and
the other parameters are conversion factors.

To include a factor of safety in the calculation, a C_∞ of 59 000 Bq/m^3 (1600 pCi/l) is assumed. This concentration is approximately three times the geometric mean concentration measured by Turk et al. (1990) in a study of Pacific Northwest homes but is lower than soil gas radon concentration in some regions of the country. The square root term is an estimated ventilation rate. Using the common method of combining natural convection and mechanical ventilation (Sherman 1990), we add a typical measured ventilation rate (0.4 air change per hour) and the ventilation caused by SSP system operation in quadrature. Equation 10 is based on a mass balance and assumes that basement and house air are uniformly mixed.

Based on calculations with Equation 10, with an SSP pit pressure of 60 Pa the indoor radon concentration is greater than the EPA guideline value of 4 pCi/l unless the medium or high permeability aggregate is selected. Maintaining a 250 Pa pressure at the SSP pit results in minimal radon entry even with the lowest permeability aggregate, however, a large fan is required and the ventilation rate of the house is increased substantially (see column 9 of Table 6).

To help elucidate the process of radon entry during SSP system operation, the radon entry rate in the absence of radon diffusion is provided in the last column of Table 6 and should be compared to the radon entry rate with diffusion. With the lowest permeability aggregate installed, there is significant radon entry even when diffusion is artificially eliminated. In these instances, the SSP system is not pressurizing the entire subslab region. Interestingly, there are situations when the radon entry rate decreases as the soil permeability decreases (for example compare the radon entry rates in the ninth and eleventh rows of numerical results). As discussed previously, only in high permeability soil are soil gas velocities sufficient to prevent diffusive radon entry into the aggregate layer. Based on our calculations with a moderate soil-gas radon concentration, this diffusion of radon into the aggregate does not lead to a substantially elevated indoor radon concentration; however, when soil gas radon concentrations are much higher than assumed for our calculations, a high soil permeability may be necessary for successful SSP system performance.

Two major conclusions can be deduced from the set of simulations described in Table 6. 1) Successful SSP system performance requires a high aggregate permeability (independent of the soil permeability), in order to position the 0 Pa isobar in the aggregate layer as close as possible to the perimeter of the slab. 2) When convective flow from the soil into the aggregate is eliminated by SSP system operation, high permeability soils improve SSP system performance due to the reduction (or elimination) of diffusive radon entry from the soil into the aggregate layer.

Table 6: Model inputs and results of parametric study of SSP system performance in the idealized house.

Soil perm. $[m^2]$	Gravel perm. $[m^2]$	Perm ratio	Pressure at the pit [Pa]	Pmin (30 cm) [Pa]	SSV Fan flow $[m^3/s]$	SSV Fan flow [cfm]	Soil-to-basement flow $[m^3/s]$	Soil-to-basement flow (2)ACH	Mass defect [%]	Rn Entry rate $[cm^3/s * (3)C_\infty]$	(1)Indoor Rn Conc. [pCi/l]	Rn Entry rate with no diffusion $[cm^3/s * (3)C_\infty]$
10^{-9}	$2.0x10^{-8}$	20	+60	-0.26	0.017	36	0.011	0.32	$3.0x10^{-6}$	120.	11.	21.
10^{-9}	10^{-7}	100	+60	9.9	0.033	70	0.021	0.62	0.03	0.09	<0.1	0.08
10^{-9}	$3.0x10^{-7}$	300	+60	20.2	0.045	95	0.029	0.85	0.01	$7.6\ 10^{-5}$	<0.1	0.
10^{-10}	$2.0x10^{-8}$	200	+60	-1.0	0.012	25	0.012	0.35	$4x10^{-6}$	58.	5.1	24.
10^{-10}	10^{-7}	1000	+60	16.	0.026	55	0.024	0.70	0.06	0.37	<0.1	0.014
10^{-11}	$2.0x10^{-8}$	2000	+60	-1.1	0.012	25	0.012	0.35	$4.x\ 10^{-6}$	55.	4.8	8.8
10^{-9}	$2.0x10^{-8}$	20	+250	14.	0.055	120	0.024	0.70	$4.x\ 10^{-3}$	2.0	.12	1.6
10^{-9}	10^{-7}	100	+250	40.0	0.09	190	0.045	1.32	0.06	0.023	<0.1	0.019
10^{-9}	$3.0x10^{-7}$	300	+250	64.	0.12	250	0.063	1.85	0.02	$1.1x10^{-7}$	<0.1	0.
10^{-10}	$2.0x10^{-8}$	200	+250	25.	0.036	76	0.031	0.91	0.02	2.88	.13	1.04
10^{-11}	$3.0x10^{-7}$	30000	+250	113	0.083	180	0.083	2.44	1.9	1.9	<0.1	0.

(1) Indoor radon concentration assuming C_∞ of 1590 pCi/l, a single zone basement and first floor house with an air exchange determined by adding in quadrature 0.4 air changes per hour and the soil-to-basement flow in m^3/h divided by the indoor volume.

(2) Equivalent air changes per hour of house assuming a total height between basement floor and house ceiling of 5 m.

(3) C_∞ is the soil-gas radon concentration far from the soil surface and the structure (i.e 1590 pCi/l = 58830 Bq/m^3).

6.3 Additional Research Results

6.3.1 Crack Size.

The parametric simulations employed a single type of crack (1mm thick L-shaped crack at the slab perimeter) and one geometry (idealized house described in Appendix A). Additional simulation results, summarized below in Table 7, show that pressure field extension improves substantially with improved sealing of the cracks. Similar results for SSP system performance can be expected because narrow (almost fully sealed) cracks offer larger resistance to the flow of soil gas, thus improving the second factor listed in section 5.2.2.

Table 7: Effect of the crack thickness on SSD pressure field extension for soil permeability of $10^{-9}\ m^2$, aggregate permeability of $10^{-7}\ m^2$ and a SSV pit pressure of -60 Pa.

crack thickness [mm]	Pmax (30 cm) [Pa]	SSD Pres. Extension Ratio	Soil-gas Entry $[m^3/s]$	Mass defect [%]
3.	-10.	0.17	0.	0.04
2.	-11.	0.19	0.	0.06
1.	-19.	0.31	0.	0.08
0.5	-27.	0.46	0.	0.1
0.2	-30.	0.50	0.	0.2

6.3.2 Location of SSV pit.

We have briefly explored the effect of locating the SSV pit closer to a corner of the basement, i.e closer to the perimeter crack. The results are shown in Table 8. As anticipated, SSD system performance deteriorates as one locates the pit closer to the corner.

Table 8: Impact of location of the pit on SSD pressure field extension for a soil permeability of $10^{-9}\ m^2$, aggregate permeability of $2x10^{-8}\ m^2$ and SSV pit pressure of -60 Pa.

location of the pit [Pa]	Pmax (30 cm) Ratio	SSD Pres. Extension $[m^3/s]$	Soil-gas Entry [%]	Mass defect
	-9.7	0.16	$1.6\ 10^{-5}$	0.02
	-7.9	0.13	$3.7\ 10^{-4}$	0.02
	-7.3	0.12	$5.9\ 10^{-4}$	0.02

6.3.3 Multiple Bays

Commonly, the basement subslab region comprises two or more bays, fully or partially separated from one another by one or more interior footers. Installation of a SSD system in one of the bays might not be adequate to mitigate radon entry in other bays. This configuration was explored with a modified House 002 geometry: the central footer has been extended in order to divide the basement into two distinct bays. The simulation assumed SSD system installation in only one bay, with a depressurization at the pit of -125 Pa. A 1.3 mm thick L-Shaped crack was assumed around the periphery of each bay. As shown in Figure 12, the bay without the SSD system is close to failure, as measured by values of Pmax (30 cm) close to -10 Pa.

We recommend one SSD system installation per bay, or ensuring excellent pressure communication in the subslab regions of the bays (for example, by allowing pressure communicating pipe segments embedded across the width of the footer).

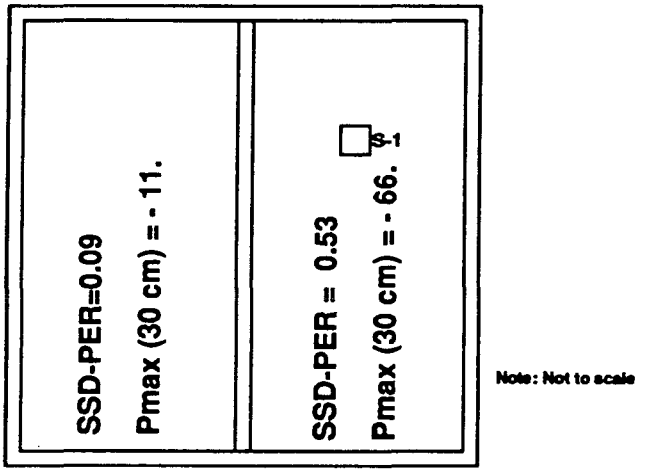

Figure 12.

SSD Pressure Extension Ratio and Pmax (30 cm) in each bay of the modified House 002 geometry. A single SSD system is in operation in the bay on the right hand-side. The pressure at the SSV pit is -125 Pa.

More research is warranted on failure-proof ways to ensure pressure communication between subslab regions of different bays, since this could obviate the need for multiple SSV systems in the same basement; leading to economic and energy savings.

6.3.4 Sub-aggregate membrane.

Improvement of SSV system performance by adding a membrane under the aggregate layer was also briefly explored. The encouraging preliminary findings are described in Appendix C.

7. Summary.

A unique field study of SSV system performance was completed in six houses with basements. For each house, the combination of soil permeability and subslab aggregate permeability was different. The field study provided data for model validation and direct evidence that SSV pressure field extension is substantially improved by a high aggregate permeability, a SSV pit, and sealing of cracks.

The permeability and Forchheimer factor of samples of three aggregate types used in the field study was measured in the laboratory. Permeability ranged from $2.x10^{-8}\,m^2$ to $3.x10^{-7}\,m^2$ and the Forchheimer factor ranged from six to twenty.

A new numerical model of SSV was developed and verified with the field data. The model accounts for non-Darcy flow in the aggregate. Non-Darcy effects were determined to significantly affect SSV performance.

Parametric simulations of SSD and SSP were completed. Based on these simulations we list our most important findings:

(1) The subslab pressure field extension resulting from SSD system operation improves substantially with increasing aggregate permeability, for the range of permeability examined. In addition, pressure field extension improves as soil permeability decreases from $10^{-9}\,m^2$ to $10^{-10}\,m^2$; however, further decreases in soil permeability have a minimal impact on pressure field extension for the cases examined. A large ratio of aggregate permeability to soil permeability reduces the need for large depressurizations at the SSV pit.

(2) A high aggregate permeability is particularly important for optimal SSP performance. To prevent convective entry of soil gas and radon into the subslab aggregate layer, the resistance to flow in the subslab aggregate must be small relative to the resistance of the cracks in the slab.

(3) Sealing of cracks and excavation of a SSV pit dramatically improves SSV pressure field extension.

The primary objective of this research was to quantify the impact of subslab aggregate permeability on SSV system performance. Providing explicit recommendations regarding the selection of a subslab aggregate among the three types considered is difficult because SSV system performance is also a function of basement characteristics (e.g. crack size and location), soil permeability, and the amount of depressurization or pressurization at the SSV pit. In the following two paragraphs, we provide quantitative summary information on the effects of increased subslab aggregate permeability. However, we must remind the reader that these quantitative results are valid only for the assumed set of conditions (e.g. basement geometry, crack size, shape and location ...).

First consider SSD system performance. If the SSD pit pressure is -60 Pa, the medium or high permeability aggregate is required to obtain an excess depressurization near the perimeter crack greater than 10 Pa. Changing from the low permeability aggregate to the medium permeability aggregate increases the SSD pressure extension ratio (SSD-PER), a measure of subslab pressure field extension, by approximately a factor of two. Switching from the medium to high permeability aggregate results in approximately another factor of 1.4 increase in SSD-PER. Selecting an aggregate, so that the ratio of aggregate permeability to soil permeability is high (e.g. 100 to 1000), substantially reduces the depressurization at the SSD pit that is required to prevent radon entry. For example, with a very high soil permeability of $10^{-9}\,m^2$, the required pressure at the SSD pit changes from -65 Pa to -20 Pa through selection of the medium permeability aggregate in place of the lowest permeability aggregate. Consequently, use of a higher permeability aggregate and operation of SSD systems with smaller depressurizations at the SSD pit, reduces the required size and energy consumption of the SSD fan and reduces the amount of ventilation caused by SSD system operation and the associated heating and cooling loads. The potential disadvantages of a higher permeability aggregate are the higher cost and the possible increased radon entry rates when SSV systems are not operated (see Appendix C).

The advantages of a high aggregate permeability discussed in the previous paragraph for SSD systems also apply for SSP systems. With a SSP pit pressure of 60 Pa, our analyses indicate that the medium or high permeability aggregate must be used in order to limit radon entry through cracks in the slab to a negligible level (i.e., to prevent indoor radon concentrations from approaching or exceeding the EPA guideline value of 4 pCi/l when the soil gas radon concentration is moderately elevated). Based on our calculations, a high aggregate permeability is even more important for SSP system performance than for SSD system performance. In addition, sealing of cracks in the slab is particularly important for effective subslab pressurization.

Finally, we note that the verified model provides us with a unique tool for further investigations of SSV system performance. Additional parametric analyses will yield more detailed information for SSV system designers.

8. Acknowledgements

This research was supported at Indoor Program of Lawrence Berkeley Laboratory by Bonneville Power Administration (BPA) through interagency agreement DE-AI79-90BP06649, and by the Assistant Secretary for Conservation and Renewable Energy, Office of Building Technologies, Building Systems and Materials Division of the U.S. Department of Energy under Contract DE-AC03-76SF00098. This research was also supported at Washington State Energy Office, Energy Extension Service by BPA Coop Agreement DE-FC79-82BO34623 Modification AO27 (WSE) 90-04). Partial support for Yves Bonnefous's research participation was granted by ENTPE of Lyon, France. We are thankful to Francis Allard of INSA of Lyon (France) and David Faulkner, Mark Modera, Ken Revzan, and Rich Sextro of LBL for their comments on the report. We gratefully acknowledge the participation in this research of Charles Cornell and Tim Nuzum of LBL, and Amy Mickelson and Mike Nuess of WEES. We also appreciate the assistance of Brian Smith of LBL in computer programming, and are thankful to Dominique Gobin of FAST, Orsay France, for his scientific advice. Finally, we thank Chuck Eastwood of BPA for technical management of this project.

References

ASTM (1984) "Standard specification for concrete aggregates" ASTM C-33-84, Published by the American Society for Testing and Materials.

Baker, P.H., Sharples, S., Ward, I.C., (1987) "Air flow through cracks", Building and Environment vol 22 No 4, pp. 293-304.

EPA (1991) "Radon resistant construction techniques for new residential construction, technical guidance". U.S. EPA, Report EPA/625/2-91/032.

Forchheimer, P.H., (1901) Z. Ver. Dtsch. Ing. 45, pp. 1782-1788.

Furman R. A. and Hintenlang, D.E. (1990) "Subslab pressure field extension studies on four test slabs typical of Florida Construction" , In: Proceedings of the 1990 International Symposium on Radon and Radon Reduction Technology, vol. V, February 19-23, Atlanta, GA. Published by the U.S. EPA, Report EPA/600/9-90/005e.

Gadgil, A. (1980) "On convective heat transfer in building energy analysis" Lawrence Berkeley Laboratory Report, LBL-10900, Berkeley, CA.

Gadsby, K.J., Reddy, A. T., Anderson, D.F., Gafgen, R. and Craig, A.B. (1991) "The effect of subslab aggregate size on pressure field extension". In: Proceedings of the 1991 International Symposium on Radon and Radon Reduction Technology, vol. 4, April 2 - 5, Philadelphia, PA. Published by the U.S. EPA.

Garbesi K. (1988) "Experiments and modeling of the soil-gas transport of volatile organic compounds into a residential basement". Lawrence Berkeley Laboratory Report, LBL-25519 Rev., Berkeley, CA.

Loureiro, C. O., Abriola, L. M., Martin, J.E., and Sextro, R.G. (1990) "Three dimensional simulation of radon transport into houses with basements under constant negative pressure". Environmental Science and Technology 24, pp. 1338-1348.

Matthews, T.G. et al. (1989) "Radon diagnostics: subslab communication and permeability measurements". In: Proceedings of the 1988 International Symposium on Radon and Radon Reduction Technology, vol. 1, October 17 - 21, 1988. Denver, CO Published by the U.S. EPA, Report EPA-600/9-89-006a.

Mowris, R.J (1986) "Analytical and numerical models for estimating the effects of exhaust ventilation on radon entry in houses with basements or crawl spaces" Lawrence

Berkeley Laboratory Report, LBL-22067, Berkeley, CA.

Nazaroff, W.W. and Nero A.V. editors (1988) Radon and its decay products in indoor air. John Wiley & Sons, New York.

Nuess, M. (1989) "Northwest residential radon standard volume 1 : project report". Bonneville Power Administration Report, Portland, OR.

Palmiter, L. and Brown, I. (1989) "Northwest residential infiltration survey: analysis and results". Ecotope, 2812 East Madison, Seattle, WA.

Patankar, S. (1980) "Numerical heat transfer and fluid flow" McGraw-Hill Book Company, New-York.

Revzan, K.L. , Fisk, W.J. (1990) "Modeling radon entry into houses with basements: the influence of structural factors", Lawrence Berkeley Laboratory Report, LBL-28109, Berkeley, CA.

Revzan, K.L., Gadgil A.J., and Fisk, W.J. (1991) "Modeling radon entry into houses with basements: model description and verification", Indoor Air 2, pp 173-189.

Scheidegger, A.E. (1960) The physics of flow through porous media. 2nd Ed., Macmillan, New-York.

Sherman, M.H. (1990) "Superposition in infiltration modeling". Lawrence Berkeley Laboratory Report, LBL-29116, Berkeley, CA. Submitted to Building and Environment.

Turk, B.H., Harrison J., and Sextro R.G. (1989) "Performance of radon control systems" Lawrence Berkeley Laboratory Report LBL-27520, Submitted to Energy and Buildings.

Turk, B.H. , Prill, R.J. , Grimsrud, D.T., Moed, B.A., and Sextro, R.G. (1990) "Characterizing the occurrence, sources, and variability of radon in Pacific Northwest homes". J. Air Waste Manage. Assoc. 40, pp. 498-506.

WSBCC [Washington State Building Code Council] (1990) "Washington State ventilation and indoor air quality code, chapter 5 radon resistive construction standards". Published by the State of Washington.

Appendices

Appendix A

A-1 The solution procedures

Dimensionless transformation

It will be useful for later computations to restate the dimensional equations of the model in term of dimensionless variables. In order to do this, all variables will be multiplied by the appropriate combinations of the following three defined characteristic parameters:

ΔP Characteristic disturbance pressure $[Pa]$

$\frac{1}{\lambda_{RN}}$ Characteristic time $[s]$ (λ_{RN} is the radon - ^{222}RN - decay constant)

D_{ch} Characteristic bulk diffusion coefficient $[m^2/s]$

Definition of the dimensionless variables

The following characteristic parameter and dimensionless variables are now defined in terms of the above set:

- Characteristic length:

$$L_{ch} = \sqrt{\frac{D_{ch}}{\lambda_{RN}}} \tag{A1}$$

- Characteristic velocity

$$V_{ch} = \sqrt{D_{ch}\lambda_{RN}} \tag{A2}$$

- Dimensionless disturbance pressure

$$^{\#}p = \frac{p}{\Delta P} \tag{A3}$$

- Dimensionless velocity vector:

$$^{\#}V = \frac{V}{V_{ch}} \tag{A4}$$

- Dimensionless coordinates:

$$^{\#}x, ^{\#}y, ^{\#}z = \frac{x}{L_{ch}}, \frac{y}{L_{ch}}, \frac{z}{L_{ch}}. \tag{A5}$$

- Dimensionless permeability

$$^{\#}k = \frac{k}{(L_{ch})^2} \tag{A6}$$

- Dimensionless viscosity

$$^{\#}\mu = \frac{\lambda_{RN}}{\Delta P}\mu \tag{A7}$$

- Dimensionless soil parameters for the Darcy-Forchheimer model:

$$^{\#}c = cV_{ch} \tag{A8}$$

- Dimensionless diffusion coefficient of radon in soil:

$$^{\#}D = \frac{D}{D_{ch}} \tag{A9}$$

- Dimensionless gradient operator:

$$^{\#}\vec{\nabla} = L_{ch}\vec{\nabla} \tag{A10}$$

Equations written in terms of dimensionless variables.

The Darcy-Forchheimer equation becomes:

$$^{\#}\vec{\nabla}^{\#}p = -\frac{^{\#}\mu}{^{\#}k}(1 + {}^{\#}c\,|^{\#}\vec{V}|)\,^{\#}\vec{V} \tag{A11}$$

The continuity equation keeps the same form as we can simplify by the characteristic parameters:

$$^{\#}\vec{\nabla}.^{\#}\vec{V} = 0 \tag{A12}$$

System to be solved:

From now, the variables we will be dealing with are dimensionless variables. We will drop the (#) notation in order to improve in clarity.

Our model will solve:
the Darcy-Forchheimer law:

$$\vec{\nabla}p = -\frac{\mu}{k}(1 + c\,|\vec{V}|)\vec{V}\ , \text{and} \tag{A13}$$

the continuity equation:

$$\vec{\nabla}.\vec{V} = 0\ . \tag{A14}$$

The solution procedures use a finite difference method, using primitive variables (i.e. fluid pressure and velocity components rather than complex versions of vorticities and stream function) and staggered grids for the pressure and the velocity. We use the Alternate Direction Implicit (ADI) method of iterative solutions.

A-2 Linearization & Discretization

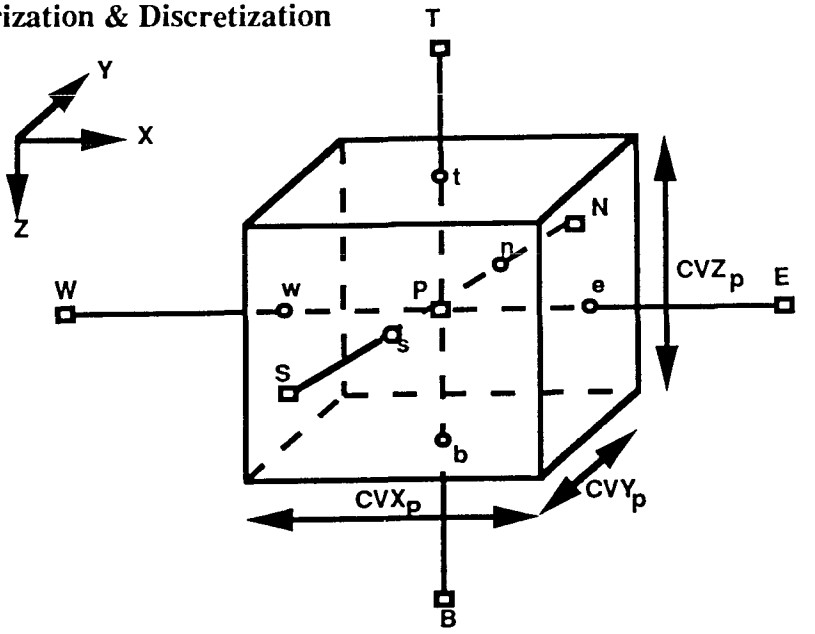

Figure A1. Control volume notation.

The above figure shows the grid notation. CVX, CVY, CVZ are the dimensions of the control volume, in the X, Y and Z directions, centered on the main grid node denoted with the subscript P. U, V, W are the velocity components along X,Y,Z directions, evaluated on staggered grid nodes which are centered on faces of the control volumes of the main grid (see Figure A1).

In the description of the iteration scheme below, the starred variables (*), represent the value of the variable at the start of the present iteration . The variables which are not starred represent the corrected value of the variable at the end of the iteration.

In the algorithm selected for the code, the equations are linearized by adding and subtracting a Darcy term. We use the SIMPLE algorithm, Semi Implicit Method for Pressure Linked Equations, as described by Patankar (1980), for obtaining closure between the pressure and the velocity calculations.

The discretization of Equation (A13) is then given by

$$U_e = -2\frac{k_e}{\mu}\left[\frac{p_E - p_P}{CVX_E + CVX_P}\right] \qquad \text{(A15)}$$

$$-2\frac{k_e}{\mu}\left[\frac{p_E^* - p_P^*}{CVX_E + CVX_P}\right]\left[\left[\frac{1}{1+\dfrac{k_E\, c_P\, Speed_P^* + k_P\, c_E\, Speed_E^*}{k_P + k_E}}\right] - 1\right]$$

where

$$k_e = \frac{K_E\, K_P\, (CVX_P + CVX_E)}{K_E\, CVX_P + K_P\, CVX_E} \quad \text{,and} \tag{A16}$$

$$Speed_P^* = \frac{1}{2}\left[(U_e + U_w)^2 + (V_n + V_s)^2 + (W_b + W_t)^2\right]^{\frac{1}{2}} . \tag{A17}$$

U_w, V_n, V_s, W_b, W_t are computed in a similar way.

The first term on the right hand side of Equation A15 is used to calculate the self-consistent pressure and velocity fields within an iteration, with the non-Darcy effects accounted for by the second term, in the square brackets, which is like a fixed source term for the velocity component in a given iteration. The full non-Darcy equation is thus solved through the iterative process.

The discretization of the continuity equation (A14) is given by

$$\frac{U_e - U_w}{CVX_P} + \frac{V_n - V_s}{CVY_P} + \frac{W_b - W_t}{CVZ_P} = 0 . \tag{A18}$$

Equation A15 into A18 yields

$$a_P\, P_P = a_E P_E + a_W P_W + a_N P_N + a_S P_S + a_B P_B + a_T P_T + b \quad , \tag{A19}$$

where

$$a_E = \frac{1}{\mu}\, \frac{2\, k_e}{CVX_P\, (CVX_E + CVX_P)} \quad , \tag{A20}$$

$$a_W = \frac{1}{\mu}\, \frac{2\, k_w}{CVX_P\, (CVX_W + CVX_P)} \quad , \tag{A21}$$

$$a_N = \frac{1}{\mu}\, \frac{2\, k_n}{CVY_P\, (CVY_N + CVY_P)} \quad , \tag{A22}$$

$$a_S = \frac{1}{\mu}\, \frac{2\, k_s}{CVY_P\, (CVY_S + CVY_P)} \quad , \tag{A23}$$

$$a_B = \frac{1}{\mu}\, \frac{2\, k_b}{CVZ_P\, (CVZ_B + CVZ_P)} \quad , \tag{A24}$$

$$a_T = \frac{1}{\mu}\, \frac{2\, k_t}{CVZ_P\, (CVZ_T + CVZ_P)} \quad , \tag{A25}$$

$$a_P = a_E + a_W + a_N + a_S + a_B + a_T \quad \text{, and} \tag{A26}$$

$$b = -\left[\frac{U_e^* - U_w^*}{CVX_P} + \frac{V_n^* - V_s^*}{CVY_P} + \frac{W_b^* - W_t^*}{CVZ_P}\right] . \tag{A27}$$

A.3) Calculation of the permeability at an interface between two control volumes.

Consider two adjacent control volumes, each containing homogeneous and isotropic media with different permeabilities. Consider flow of fluid under a pressure gradient across these control volumes. The simple analogy to this problem is current flow through two resistances in series. Figure A2 shows the electrical analog problem:

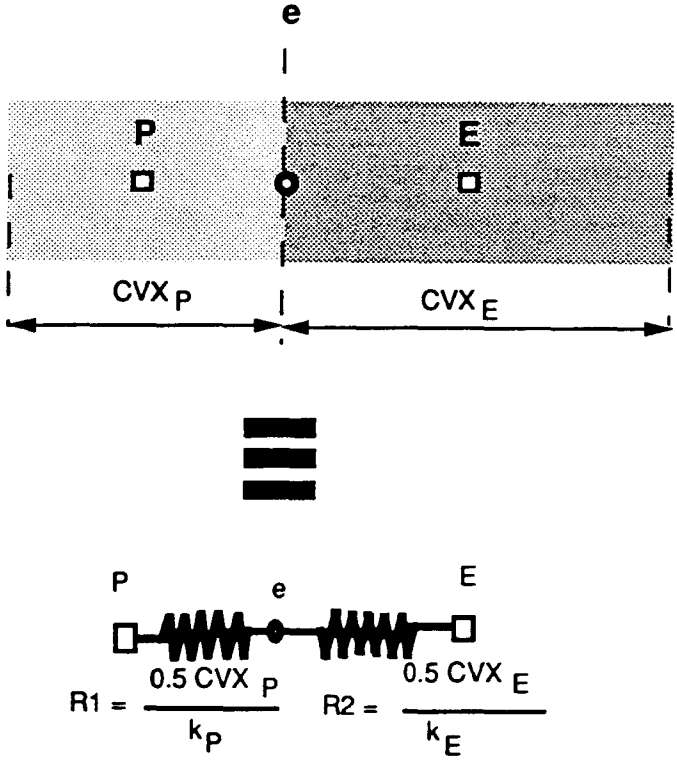

Figure A2.
Electrical analog of two adjacent control volumes.

We know that $\frac{1}{conduc\,1\&2} = \frac{1}{conduc\,1} + \frac{1}{conduc\,2}$,

so

$$\frac{0.5(CVX_E + CVX_P)}{k_e} = \frac{0.5\,CVX_P}{k_P} + \frac{0.5\,CVX_E}{k_E} \tag{A28}$$

which gives

$$k_e = \frac{k_E\,k_P}{\frac{k_E\,CVX_P + k_P\,CVX_E}{CVX_E + CVX_P}} \,. \tag{A29}$$

A.4) Calculation of the Darcy-Forchheimer expression at an interface between two control volumes.

We solve here the one-dimensional problem and will assume that the result is applicable for each direction of the three-dimensional model. The grid notation is shown in Figure A3.

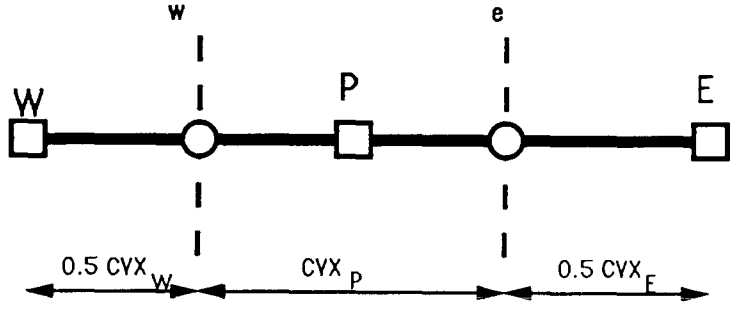

Figure A3. Grid notation along the X-axis.

For clarity we will deal with the general Darcy-Forchheimer law.

The continuity equation implies the velocity to be a constant. Then; from Equation A13, we have

$$(1 + c_P\ Speed_P)\ U = -\frac{k_P}{\mu}\ \frac{p_e - p_P}{0.5\ CVX_P} \tag{A30}$$

and

$$(1 + c_E\ Speed_E)\ U = -\frac{k_E}{\mu}\ \frac{p_E - p_e}{0.5\ CVX_E}\ . \tag{A31}$$

Eliminating p_e between Equations (A30) and (A31), we get

$$-\left[\frac{0.5\ CVX_P\ \mu}{k_P}\ (1 + c_P\ Speed_P) + \frac{0.5 CVX_E\ \mu}{k_E}\ (1 + c_E\ Speed_E)\right] U = p_E - p_P\ , \tag{A32}$$

which can be rearranged as

$$\left[1 + \frac{CVX_P\ k_E\ c_P\ Speed_P + CVX_E\ k_P\ c_E\ Speed_E}{CVX_P\ k_E + CVX_E\ k_P}\right] U = \frac{1}{\mu}\ \frac{-k_E\ k_P}{\dfrac{k_P\ CVX_E + k_E\ CVX_P}{CVX_P + CVX_E}}\left[\frac{p_E - p_P}{0.5(CVX_P + CVX_E)}\right], \tag{A33}$$

and finally as

$$\left[1 + \frac{CVX_P\ k_E\ c_P\ Speed_P + CVX_E\ k_P\ c_E\ Speed_E}{CVX_P\ k_E + CVX_E\ k_P}\right] U = -2\ \frac{k_e}{\mu}\left[\frac{p_E - p_P}{CVX_P + CVX_E}\right], \tag{A34}$$

where

$$k_e = \frac{k_P\ k_E}{(k_P\ CVX_E + k_E\ CVX_P)\ /\ (CVX_P + CVX_E)}\ . \tag{A35}$$

Note that this is consistent with Equation (A29)

A.5) Boundary conditions at the L-shaped slab-footer crack.

This section of the appendix describes the boundary conditions imposed at the interfaces between the crack and the soil or between the crack and the concrete.

Figure A4 shows the L-shaped crack defined at the basement slab-footer joint, and the first control volume in the sub-slab region next to the crack. Also shown are the interface between the crack and the control volume in the sub-floor region and the interface between the crack and the air volume inside the basement.

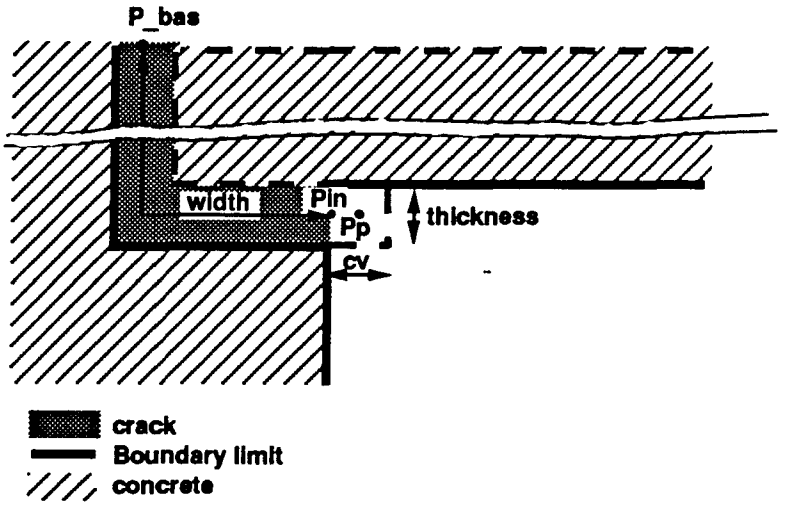

Figure A4.
Vertical cross section of a slab-footer crack.
The crack is shown greatly exaggerated.

At the soil-side boundary of the crack, the disturbance pressure and the velocity of the soil gas through the interface are continuous functions of distance. Consider a point (IN) located right at the interface. Then, for a point $(IN-)$ located inside the crack but very close to the point (IN), and for a point $(IN+)$ located in the soil, but very close to the point (IN), the boundary conditions are expressed as

$$p_{(IN-)} = p_{(IN+)} = p_{(IN)} \tag{A36}$$

$$v_{(IN-)} = v_{(IN+)} = v_{(IN)} \ , \tag{A37}$$

where

$p_{(IN-)}$ =Limiting value of the disturbance pressure within the crack close to the interface;

$p_{(IN+)}$ =Limiting value of the disturbance pressure within the control volume in the soil close to the interface; and

$v_{(IN-)}$ =Limiting value of average velocity of the soil gas within the crack close to the interface;

$v_{(IN+)}$ =Limiting value of average velocity of the soil gas within the control volume of the soil close to the interface.

The crack is modeled with one control volume whose characteristics (equivalent permeability, equivalent Forchheimer term) are determined by matching equation of flow within an L-shaped crack to a Darcy-Forhheimer law. Once this identification is carried out, the control volume representing the crack is treated just like others, but with its own values for permeability and Forchheimer factors. Continuity of velocity and pressure fields at the "soil/crack" interface is ensured like at any other interface between two adjacent control volumes.

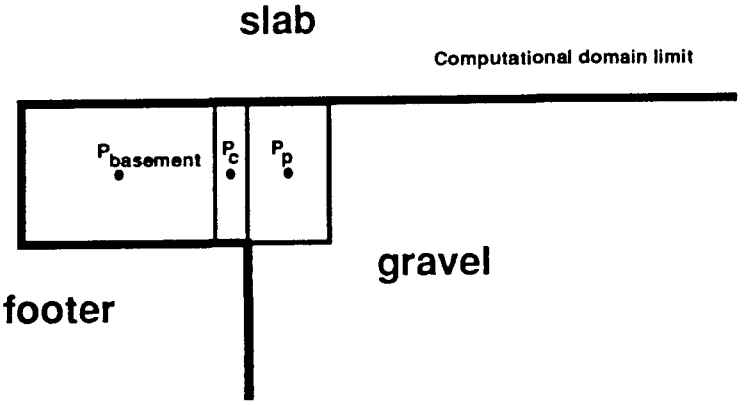

Figure A5.
Vertical cross section of the slab-footer crack
as modeled by a control volume.

The size of the control volumes are chosen in order to reduce to a negligible magnitude the effect of the crack permeability on the pressure drop in between P_{crack} and P_P

The relationship between the velocity in an L-shaped crack and the pressure differential between the two sides of the crack can be expressed by (from Baker et al. (1989))

$$p_{(IN)} - p_{bas} = Coeff_1 \, v_{(IN-)} + Coeff_2 \, |v_{(IN-)}| \, v_{(IN-)} \, , \qquad \text{(A38)}$$

where

$Coeff_1$= $\dfrac{12\mu width}{thickness^2}$, and

$Coeff_2$= $1.25\rho_0$.

The Darcy-Forchheimer equation gives the relationship between the pressure field

and the velocity field within a porous media

$$p_P - p_{(IN)} = -Coeff_3 \, v_{(IN+)} \,, \tag{A39}$$

where

$$Coeff_3 = \frac{\mu}{k}(1 + c\ Speed\ ) * L$$

and L is the distance between P_{crack} and P_p (see Figure A5).

By identification of Equation A38 to Equation A39, we get

$$K_{crack} = L\ \frac{Thickness^2}{12\ width} \,, \text{and} \tag{A40}$$

$$c_{crack} = \frac{1.25\ \rho_0\ Thickness^2}{12\ \mu\ width} \,. \tag{A41}$$

Where K_{crack} and c_{crack} are equivalent crack permeabilities and Forchheimer terms. Some values of these parameters for various crack thickness are provided in Table A1.

Table A1: Permeabilities and Forchheimer terms used to characterize cracks.

Crack Thickness [mm]	K_{crack} $[m^2]$	c_{crack} [s/m]
3.	3.75×10^{-7}	0.31
2.	1.7×10^{-7}	0.14
1.	4.2×10^{-8}	0.035
0.5	1.0×10^{-8}	0.0083
0.2	1.7×10^{-9}	0.0014

Note: Calculations done for:
L=0.1 m
$width$=0.2 m

This model for the crack is tentative. It is well understood that the slab-footer joint is not a regular L-shaped crack. While the overall shape is not incorrect, in reality they are likely to be irregularly shaped (non-smooth) walls, rounded corners, and an uneven crack thickness.

A.6) Geometrical configuration of the model

House 002

For the numerical modeling, we use House 002 geometry with the following simplifications:

- The garage floor is modeled as an impermeable surface.
- The junction between the main basement and the half-depth basement is modeled as an open joint (see Figure A6, Section B-B).
- The location of garage and half-depth basement have been slightly modified by ignoring their small offsets with the main basement. This aligning of boundaries has allowed us considerable increase in simulation speed by reducing the number of grid nodes.
- The staircase connecting the half-depth basement to the main basement has been omitted from the model for similar reasons.
- A rectangular SSV pit is assumed.
- We assumed that the basement wall is thicker than it actually is so that the outdoor surface of the wall lines up with the outer edge of the footer.

Figures A6a through A6d show the layout of the computational domain for modeling House 002.

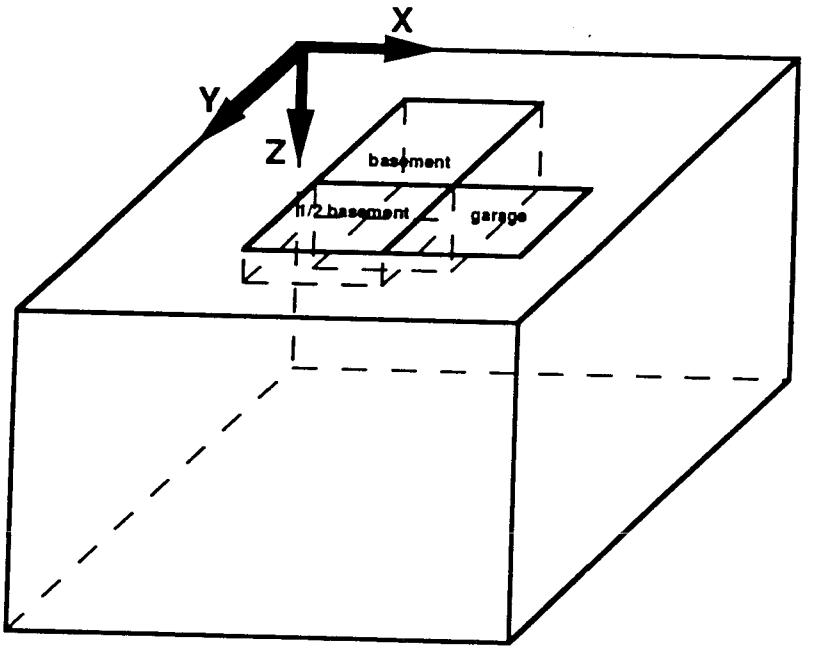

Figure A6a.
Schematic representation of the soil block and House 002.

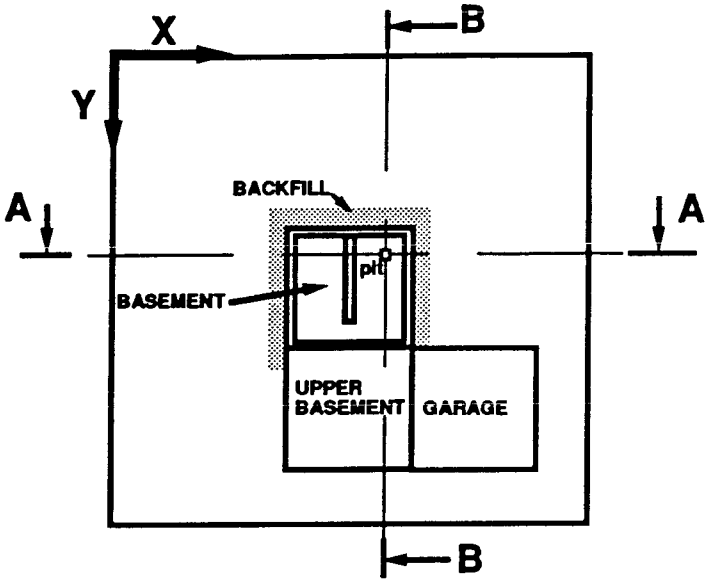

Figure A6b.
Plan view of House 002.

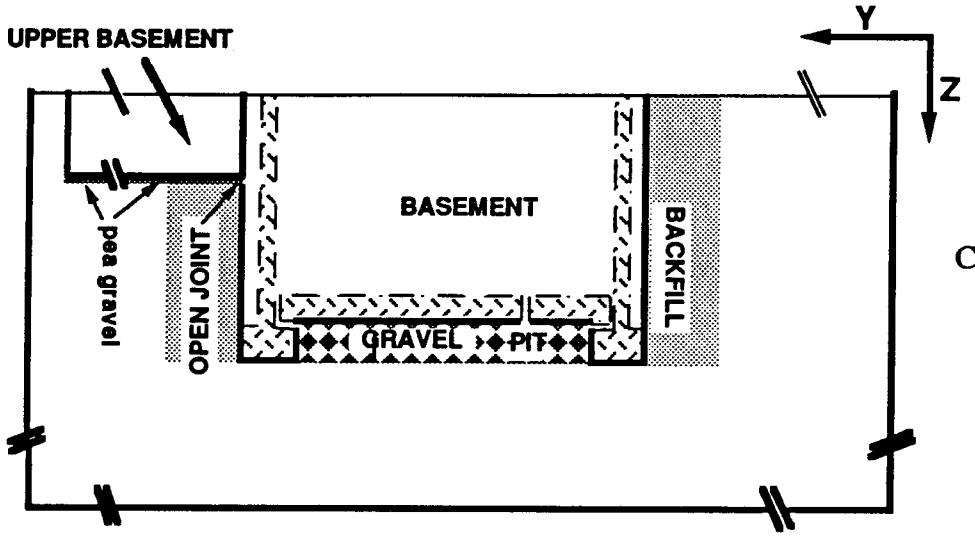

Figure A6c.
Cross section B-B of House 002.

Section BB

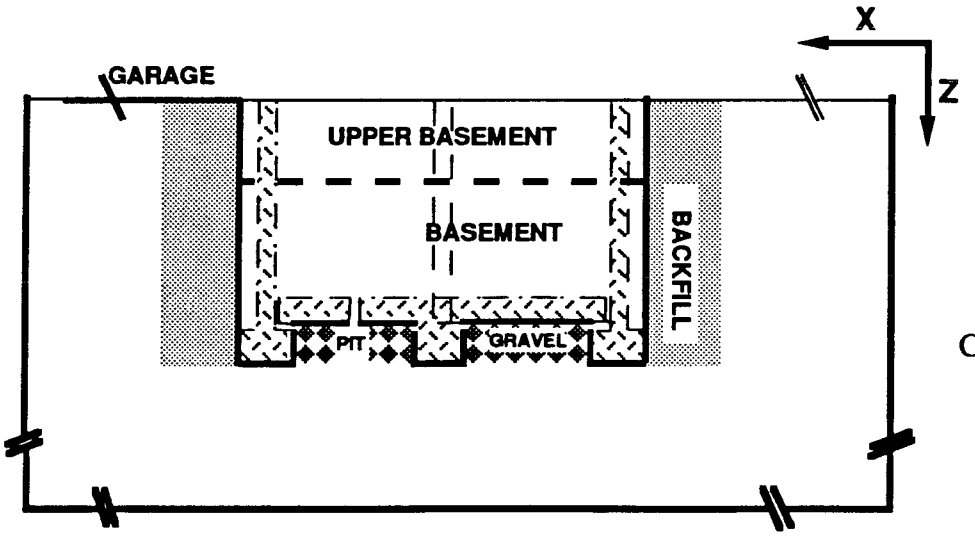

Figure A6d.
Cross section A-A of House 002.

Section AA

House 003

Similarly, House 003 geometry has been simplified as follows:

- The middle footer location has been slightly modified by ignoring its small offset with the "hasty footing" and the staircase north wall footer.
- The window well has been omitted.
- The west solid concrete slab extension (8 square feet) has been neglected.

Figure A7 shows the layout of the computational domain for House 003

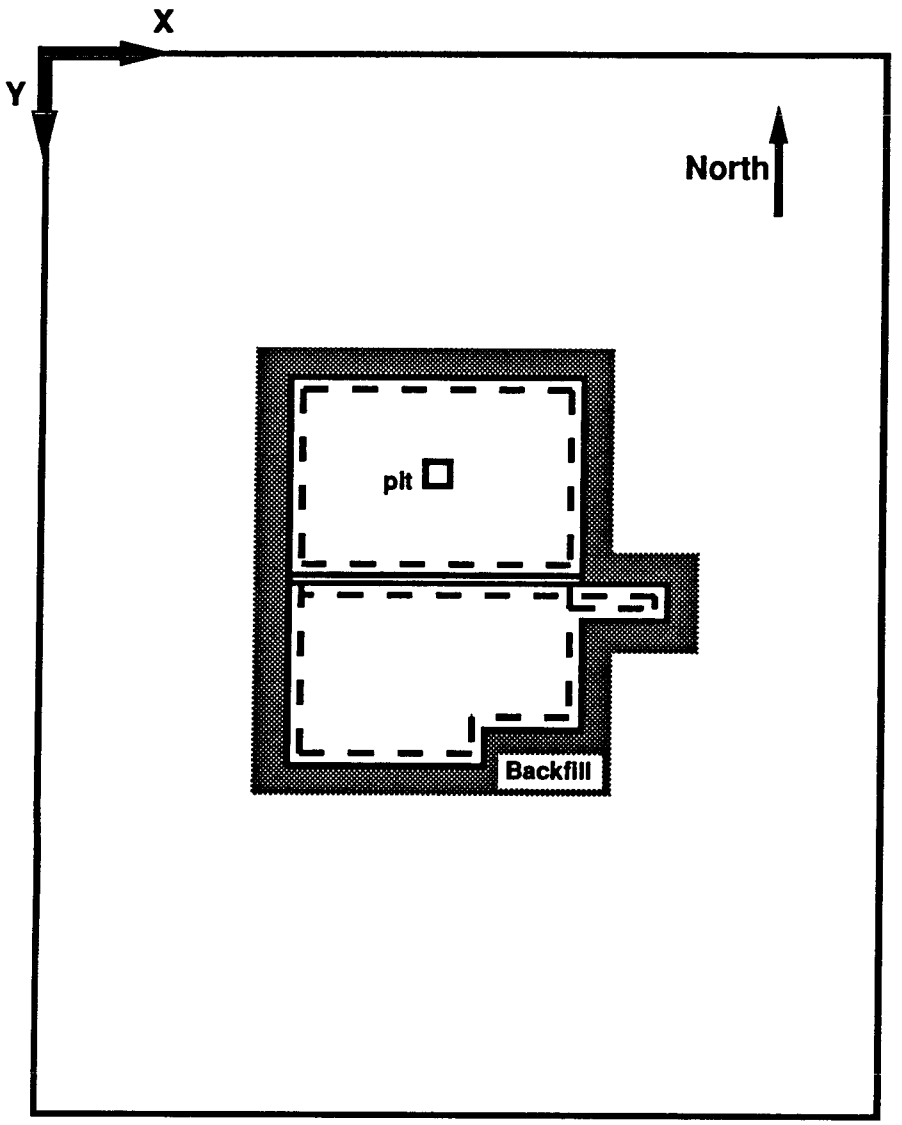

Figure A7.
Plan view of House 003.

Idealized house.

The parametric simulations are based on the geometry for an idealized house described here. The geometry selected is a rectangular house with a complete center footing dividing the sub-slab region into two bays, with a garage at the ground level on the side. This configuration allows us to use the plane of symmetry in the vertical section of the center footing and to model only half of the domain. Reducing the number of grid nodes by half allowed us considerable increase in simulation speed.

Figures A8a and A8b show the layout of the computational domain for the idealized house.

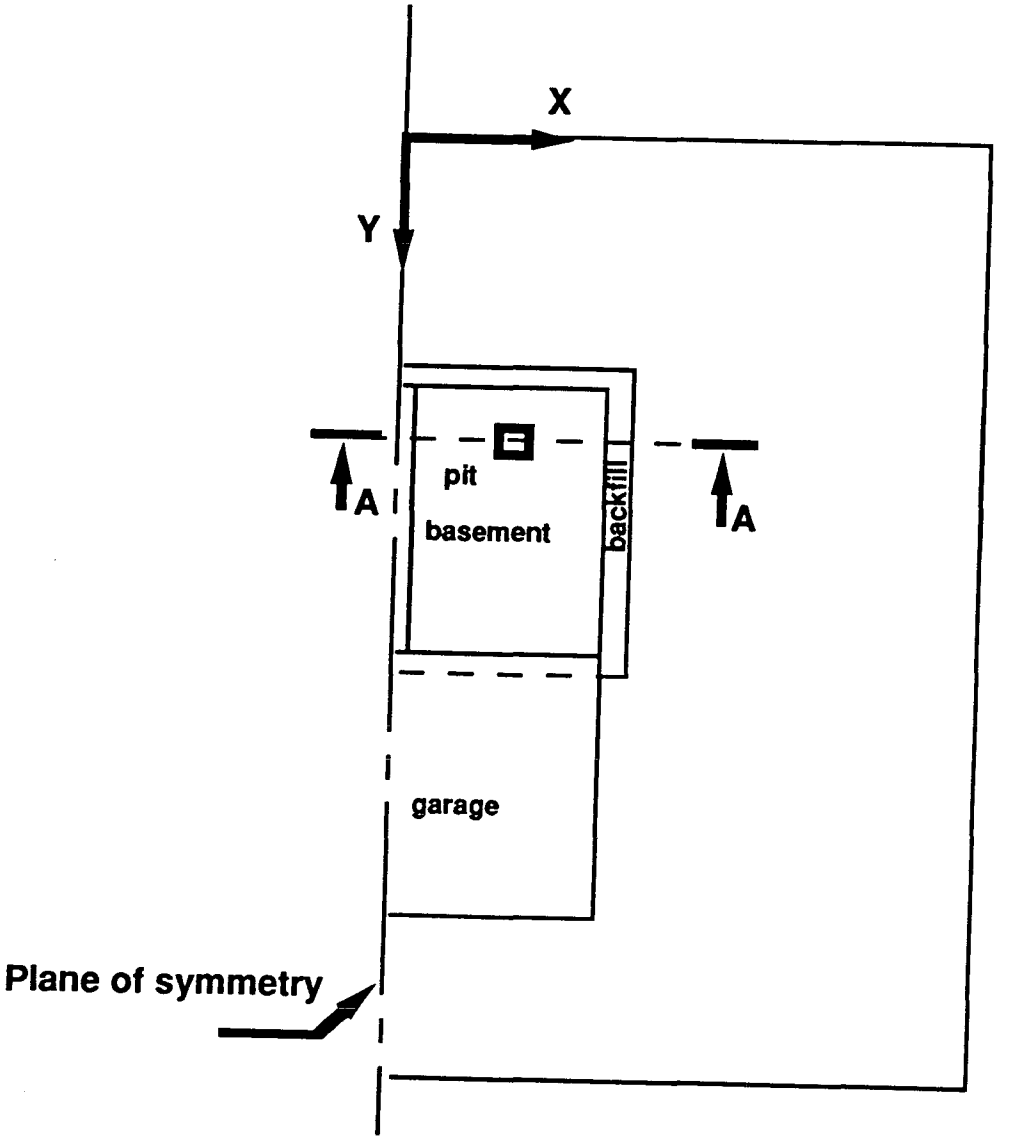

Figure A8a.
Plan view of idealized house.

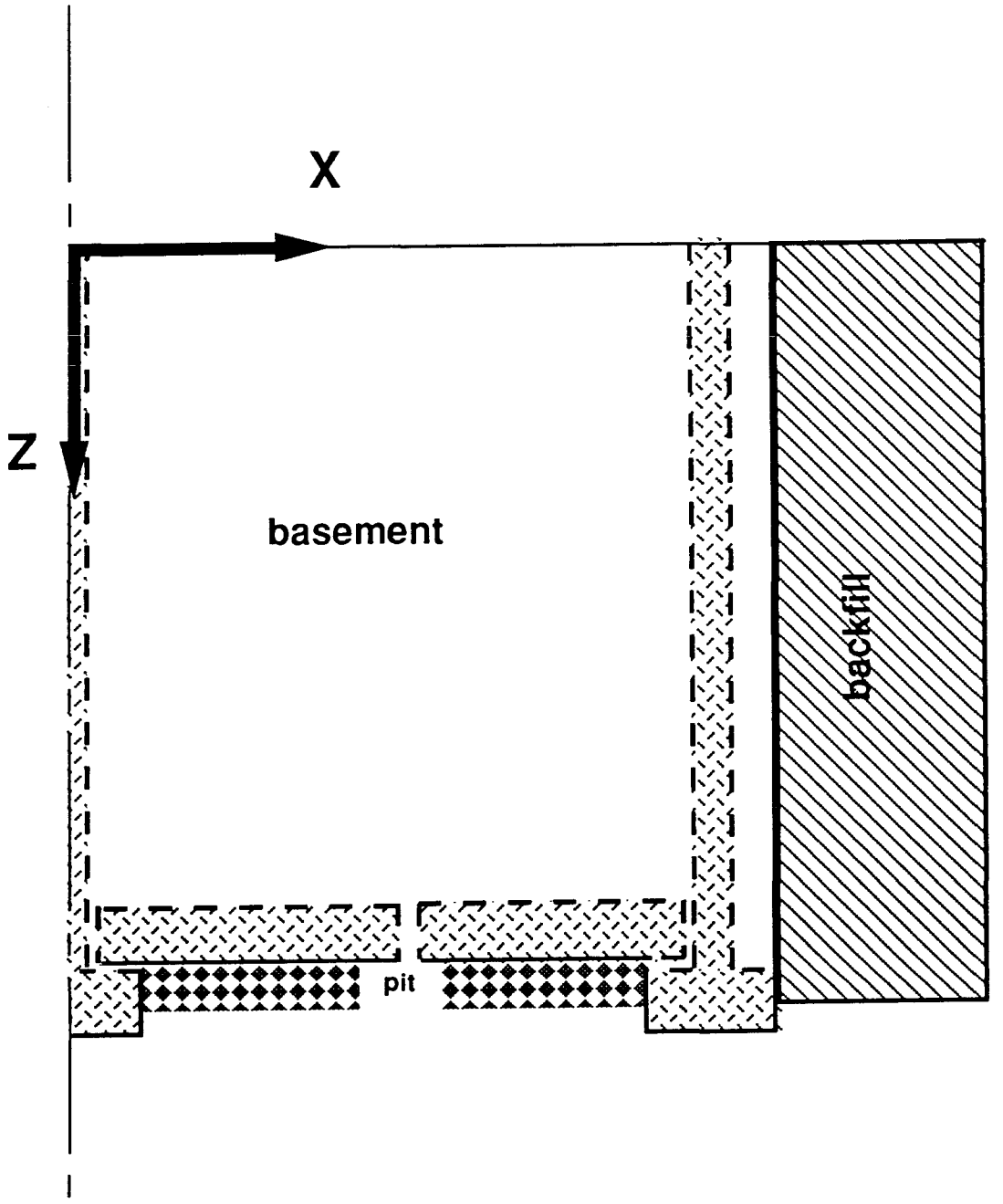

Figure A8b.
Cross section A-A of idealized house.

Appendix B

Methods and Results of Aggregate Characterization

Background and Objectives

The relationship between pressure gradient and air velocity when air flows through the three types of aggregate was measured in the laboratory. This information is required as an input for the numerical model of subslab ventilation. We were required to characterize this relationship for a wide range of air velocities corresponding to the velocities in subslab aggregate layers when subslab ventilation systems are operating.

At the lowest velocities, we expect a linear relationship between pressure gradient and velocity (i.e., Darcy Flow). This relationship can be expressed by a rearranged version of Darcy's Law for one dimensional flow

$$\frac{\Delta P}{L} = \frac{\mu}{K} V \tag{B1}$$

where: ΔP is the pressure drop, L is the length in the direction of flow, K is the gravel permeability, μ is the dynamic viscosity of the fluid, and V is the bulk velocity. Darcy's Law is generally considered valid for flow of a non-adsorbing gas through a permeable media if the associated Reynolds Number is below some limit which ranges from 0.1 to 75 based on previous experimental data (Scheidegger 1960). The Reynolds Number (Re) is defined as follows

$$\mathrm{Re} = \frac{V D_P \rho}{\varepsilon \mu} \tag{B2}$$

where: D_P is the particle size, ρ is the fluid density, ε is the porosity of the permeable media, and the other parameters are as previously defined. The value of D_P is not clearly defined for a media such as aggregate with a range of particle sizes; however, we use estimates of typical particle sizes to determine approximate values for Re.

The Darcy Forchheimer equation relates pressure gradient and velocity over a larger range of velocities, i.e.,

$$\frac{\Delta P}{L} = \frac{\mu}{K} V + c \frac{\mu}{K} V^2 \tag{B3}$$

where c is a constant called the Forchheimer factor. Dividing the equation by V yields

$$\frac{\Delta P}{L\,V} = \frac{\mu}{K} + c\,\frac{\mu}{K}\,V \tag{B4}$$

If the data are adequately represented by this equation, a plot of $\frac{\Delta P}{L\,V}$ versus V should yield a straight line.

Measurement Apparatus and Methods

We considered test configurations with flow through a horizontal channel and, alternately, a vertical column of aggregate. We were concerned that fine particles might concentrate at the lower end of a vertical column resulting in a low-permeability layer through which the air must flow. In contrast, flow through a horizontal channel mimics the flow in subslab aggregate layers and any settling of fine particles should have a similar impact on the resistance to flow in both of these situations. Therefore, we selected the configuration of horizontal flow through a channel.

The test apparatus is shown schematically in Figure B1. A plywood test box was constructed with an inlet plenum, a central section filled with aggregate, and an outlet plenum. Extensive sealing of joints and coating of surfaces were required to minimize air leakage between the interior of the box and the surroundings. Air first enters the inlet plenum which contains 30 cm long sections of 3.2 cm outer diameter plastic pipe that serve as flow straighteners. A static pressure tap (the static pressure leg of a Pitot-static tube) is located downstream of the flow straightener and immediately upstream of a screen at the upstream end of the aggregate. The flow then enters the aggregate-filled central section with an aggregate cross section of 0.222 m by 0.254 m and length of 2.43 m. A layer of compressible closed-cell foam fits between the top of the aggregate and the removable lid and eliminates an air gap at this junction. Air exiting the aggregate passes through another screen, which supports the aggregate, and flows into the outlet plenum which contains another static pressure tap.

To determine the bulk air velocities, we measured the rate of air flow entering or exiting the test apparatus and divided by the cross sectional area of the aggregate. Because measurements were required over a large range of air flow rate, two different approaches were required to drive the air flow and measure the air flow rate (see the two configurations depicted in Figure B1). For tests with a low flow, laboratory compressed air passed through a dry test meter (used for flow rate measurement) and into the inlet plenum. Two different size dry test meters with maximum rated flows of approximately 50 L/min and 120 L/min were used for measurements in the "low-velocity" and "mid-velocity" range respectively. For higher flow rates, a fan drew air through the test apparatus and through an orifice plate flow meter. Two different size orifice plates were used for measurements in the "high-velocity" and "peak-velocity" ranges, respectively. Data collected with the different flow meters overlapped to allow intercomparison. The estimated maximum error in flow rate measurements is 5%. However, we estimate that

air leakage into or out of the test box may have caused the flow rate through the test box to differ by as much as 10 % from the flow through the flow meter during tests of the lowest permeability aggregate. (Leakage was negligible during testing of the most permeable aggregate because of lower pressures in the test box). Consequently our measured velocities could have errors as high as 15%.

The static pressure (relative to room pressure) was measured upstream of the aggregate, downstream of the aggregate, inside the dry test meter, and upstream of the orifice plate. In addition, the pressure differences between the upstream and downstream ends of the aggregate and across the orifice plate were measured directly. Because of the wide range of pressures, three different measurement devices were used. When possible, each pressure measurement was repeated using a second device. A micromanometer that uses a micrometer and electronic circuitry to detect fluid level was used to measure pressure differences smaller than 500 Pa. This device has a resolution of approximately 0.5 Pa. Pressure differences smaller than 150 Pa were also measured with an electronic pressure transducer (Validyne Model DP-103) calibrated with the micromanometer (this electronic pressure transducer has a resolution better than 0.1 Pa). Larger pressure differences were measured with another multi-range electronic pressure transducer (Neotronics EDM) with a resolution of 0.1 Pa.

With the lowest air velocities in the most permeable aggregate (i.e., under conditions with a low Reynolds Number typical of Darcy flow), the pressure drops between the inlet and outlet of the aggregate bed were too low for accurate measurements. For increased measurement accuracy at low values of Reynolds Number, we also conducted tests with helium flowing through the aggregate. Helium and air have approximately the same viscosity yielding approximately the same pressure drop for a given velocity. However, the density of helium is approximately one tenth the density of air, thus the Reynolds Number for a particular velocity is approximately one tenth as high with helium.

Results

Table B1 provides information on the distribution of particle sizes for each type of aggregate as well as ASTM specifications for the corresponding class of aggregate. The information on particle sizes was provided by the companies that sell the aggregate. Because of the variation in the particle size distribution between aggregates, a large range in aggregate permeability was expected.

Figures B2, B3, and B4 are plots of the data from tests of a sample of the aggregate (called 3/4" round) used in House No. 005 of the field experiments. Figure B2 shows pressure gradient plotted versus velocity for the entire range of velocities. Because of the large range of velocities, individual low-velocity and mid-velocity data points are not distinct. The deviation from linearity is clearly evident except at the lowest air velocities.

Figure B3 shows a plot of pressure gradient versus velocity from the low- and mid-velocity tests with flow measured via the two dry test meters. The four or five lowest velocity data points indicate a linear relationship characteristic of Darcy flow. Using Equation B1 and the slope of a line fit through the four lowest velocity data points (plus the origin) yields a permeability of 1.3×10^{-7} m^2. Assuming a typical particle diameter of 0.011 m (7/16 in, see Table B1) and a typical gravel porosity of 0.4, we show values of Reynolds Number for two data points on the figure. The deviation from Darcy flow becomes evident (visually) with a Reynolds Number between 12 and 20.

Figure B4 is a plot of pressure gradient divided by velocity versus velocity (see Equation B4) for all data points. Because the data points on this figure are fit reasonably well by a straight line, the Darcy Forchheimer equation is appropriate for characterizing the flow. The low- and mid-velocity data collected using dry test meters to measure flow rate fall somewhat below the fits to the higher velocity data. We have not yet determined the causes of this discrepancy but suspect that measurement error and air leakage into the test box during peak/high-velocity tests and out of the test box during low/mid-velocity tests may explain some of the discrepancy. Straight line fits to the peak-velocity and high-velocity data points are shown on Figure B4 along with the corresponding values of permeability and Forchheimer factor computed from Equation B4. These curve fits yield slightly lower permeabilities (0.9×10^{-7} m^2 and 1.0 10^{-7} m^2) than the lowest velocity data discussed in the previous paragraph (1.3×10^{-7} m^2); however, the maximum deviation between these measured values is only 40% which is small compared to the fifteen-fold range in permeability for the three aggregate types. We use a permeability of 1.0×10^{-7} m^2 for our modeling.

The curve fits on Figure B4 to the peak- and high-velocity data, respectively, result in Forchheimer factors of 8.0 and 9.8 s/m. Similar curve fits (not shown) to the low-velocity and mid-velocity data yield Forchheimer factors of 15.5 and 16.8, respectively. Consequently, there is considerable uncertainty in the Forchheimer factor. We selected an intermediate value of 13 for our computer modeling.

Similar plotting and data analyses were completed based on the tests of the other two types of aggregate. Table B2 provides the resultant permeabilities and Forchheimer factors. For the three aggregates, permeability ranges over a factor of 15 and the Forchheimer factor ranges from six to twenty.

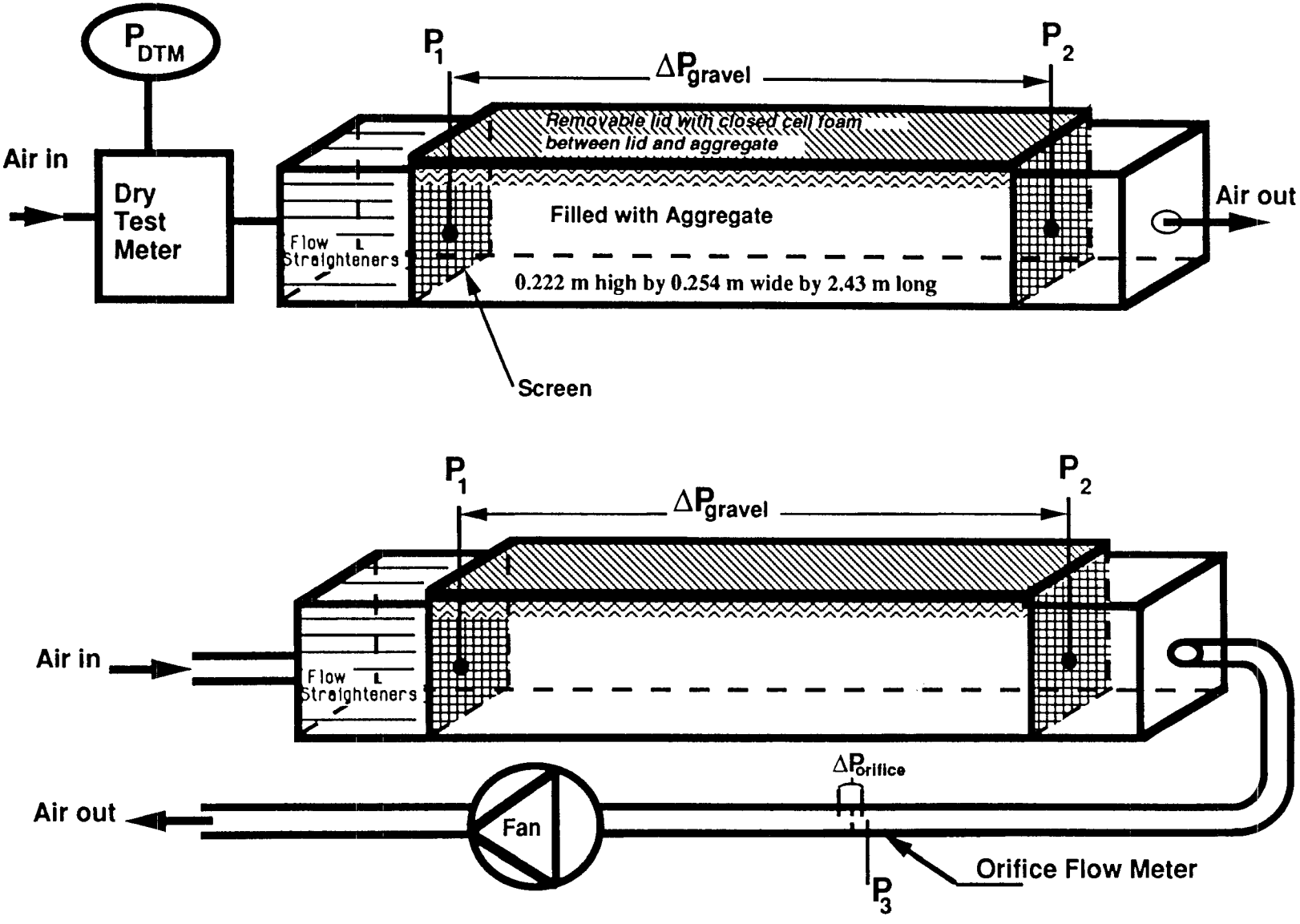

Figure B1. Schematic diagrams of the test apparatus. Low/mid and high/peak velocity data were collected using dry test meters and orifice plate flow meters, respectively, to measure flow rate.

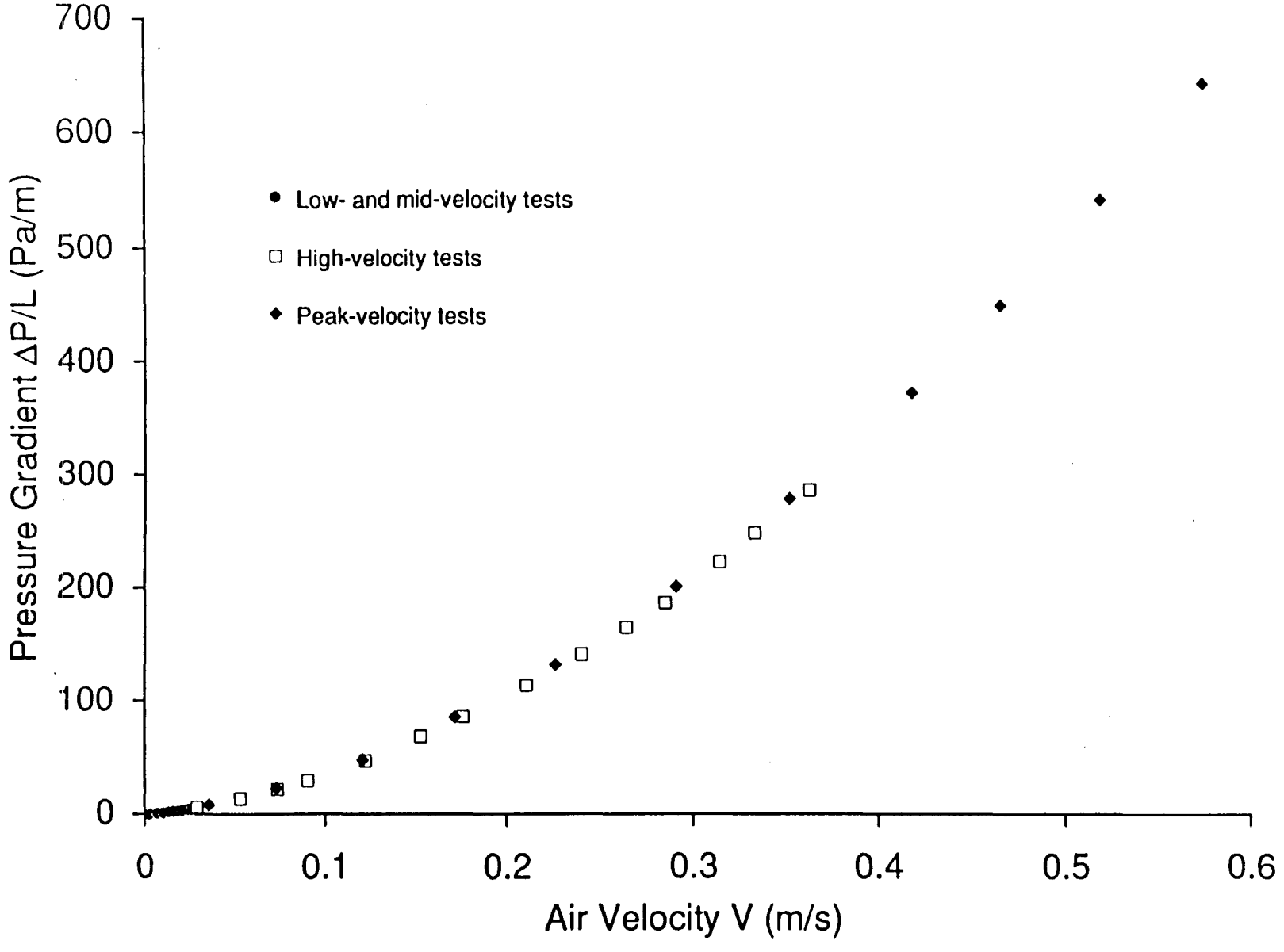

Figure B2. Full range of measured pressure gradient versus air velocity data for 3/4" round aggregate (approximate ASTM Size 67). Low-velocity and mid-velocity data points are indistinct on this figure but are shown clearly on Figure B3.

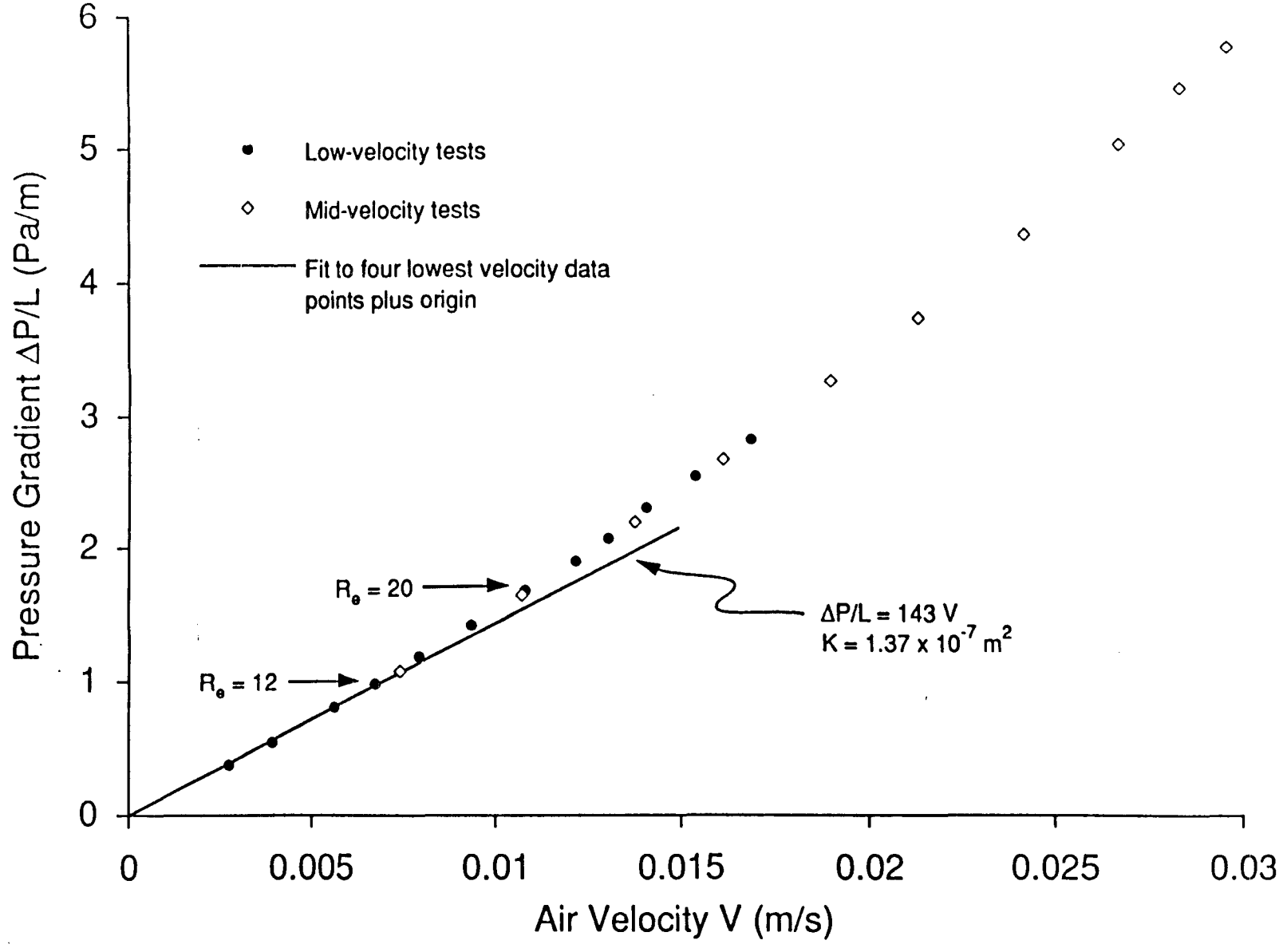

Figure B3. Measured pressure gradient versus air velocity data for 3/4" round aggregate (approximate ASTM Size 67). Only the low-velocity and mid-velocity data are included. The Reynolds Numbers are computed assuming a typical particle size of 0.011 (7/16") and a porosity of 0.4.

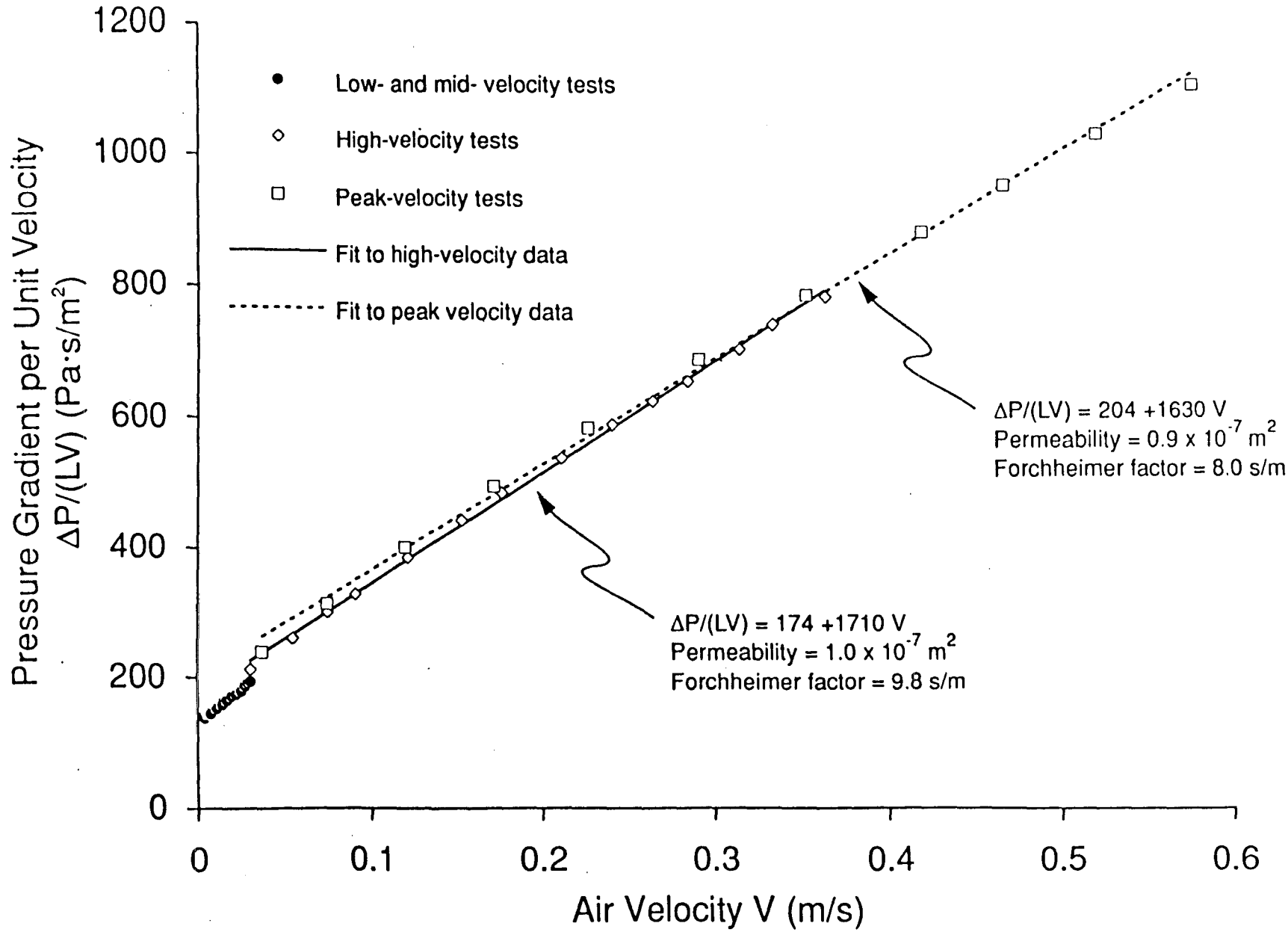

Figure B4. Measured pressure gradient per unit air velocity versus velocity for 3/4" round aggregate (approximate ASTM Size 67). The straight lines are fits to peak-velocity and high-velocity data with flow rates measured using the large and small orifice plates, respectively.

Table B1. Aggregate size data (supplied by vendors) and ASTM specifications for sizes 4,67 and 8 aggregate.

House No.	Vendor's Aggregate Name	Approx. ASTM No.	Sieve Size (square openings) 2" 50 mm	1 1/2" 37.5 mm	1" 25 mm	3/4" 19.0 mm	1/2" 12.5 mm	3/8" 9.5 mm	No. 4 4.75 mm	No. 8 2.36 mm	No. 16 1.18 mm
001	3/4" Round	67				94%	47%	25%	0.9%	0.2%	
002	1 1/2" Round	4		100%		2%		0.3%			
003	3/8" Round	8					100%	99.5%	15.4%		
004	1 3/4" Round	4		92%	51%	9%	1%	0.4%	0.4%		
005	3/4" Round	67				93%	45%	24%	1.7%	0.1%	
006	#8 Pea Gravel	8					100%	100%	40%	5%	2%
	ASTM Specifications	4	100%	90-100%	20-55%	0-15%		0-5%			
		67			100%	90-100%	20-55%	0-15%	0-5%		
		8					100%	85-100%	10-30%	0-10%	0-5%

Measured or Specified Weight % Passing Through Sieve

Table B2. Measured Permeabilities and Forchheimer Factors of Aggregate Samples.

House No.	Vendor's Aggregate Name	Approx. ASTM No.	Permeability (m^2)	Forchheimer Factor (s/m)
002	1 1/2" Round	4	3×10^{-7}	20
005	3/4" Round	67	1×10^{-7}	13
003	3/8" Exposed	8	2×10^{-8}	6

Appendix C

Impact of a membrane under the aggregate layer.

Background and Objectives

To facilitate the effectiveness of a SSV system (should one be needed), a common recommendation is to install a layer of high permeability aggregate on the site beneath the floor slab of the basement (EPA 1991, WSBCC 1991, Nuess 1989). This recommendation will result in the installation of subslab aggregate beneath the slab floors of a higher number of houses. Subslab aggregate is sometimes installed irregardless of radon-related recommendations to help prevent water entry into the basement from the soil. However, a more permeable aggregate may be selected to facilitate SSV operation.

Revzan and Fisk (1990) have shown, based on computer model predictions which have not yet been validated, that installation of subslab aggregate, compared to the case of no aggregate, may increase the rate of radon entry into a basement in the absence of a SSV system by as much as a factor of 5. Smaller, but still significant increases in radon entry rates are predicted to result from increases in aggregate permeability. For example, with soil permeabilities of $10^{-11}\,m^2$ and $10^{-10}\,m^2$, changing the permeability of the subslab aggregate from $10^{-9}\,m^2$ to $10^{-8}\,m^2$ results in predicted increases in the radon entry rate of 5% and 40%, respectively. As a consequence, the addition of subslab aggregate and, to a lesser extent, increases in aggregate permeability may increase the number of houses needing active radon mitigation systems. In other houses, radon concentrations may increase but remain below the 4 pCi/l guideline defined by EPA, resulting in increased occupant exposure to radon and increased risks of lung cancer.

This appendix provides a very preliminary evaluation of the effectiveness of a membrane under the subslab aggregate in countering these increases in radon entry rates.

Simulation procedure and results

We first modeled an idealized house, described in Appendix A, but without an aggregate layer and without a SSV system. The pressure inside the basement was maintained at -10 Pa, the perimeter crack was a 1 mm L-shaped crack, the soil permeability was set to $10^{-9}\,m^2$. Then, we added a 10 cm thick layer of #8 aggregate (see Appendix C), and ran the non-Darcy STAR code. The radon entry rate increased by a factor of 2.1. For the third simulation, we added a membrane with a 1 cm wide gap at the periphery, beneath the aggregate layer. The predicted radon entry rate decreased by 30% yielding an entry rate that is 150% of the predicted entry without subslab aggregate. Hence, in this situation, the membrane beneath the subslab aggregate partially counteracted the radon entry

increase resulting from installation of the aggregate layer. A last simulation was run after adding a SSV system with a 25 cm radius hemispherical pit, and a -60 Pa applied pressure at the suction hole. SSD operation was shown to be effective as no soil-gas entered the basement. The result from this final simulation is compared with the result of a prior simulation of SSD operation in the same idealized house with the same aggregate and soil, but without the membrane. In the prior simulation, the SSD system failed to prevent soil-gas entry into the basement at some locations. As expected, the membrane improves the SSD performance. Additional field experiments in houses with a membrane beneath the aggregate performed by the Washington State Energy Office, Washington Energy Extension Service confirm that the membrane improves SSV performance. However, these experiments are not within the scope of the present study and are not discussed further. Table C1 summarizes the results from this set of simulations.

Table C1: Evaluation of a membrane as a passive counter effect to radon entry enhancement due to a subslab aggregate layer.

	Pmax (30 cm) [Pa]	Soil-gas Entry $[m^3/s]$	Mass defect [%]	Rn ENTRY rate $[cm^3/s * C_\infty]$	Rn Entry rate with no diffusion $[cm^3/s * C_\infty]$
(1)	-1.8	9.8×10^{-4}	0.001	620.	620.
(2)	-5.2	2.9×10^{-3}	0.04	1300	1300
(3)	-7.3	1.8×10^{-3}	0.2	920	930
(4)	-12.	0.	0.04	0.	0.
(5)	-9.7	1.6×10^{-5}	0.02	0.9	1.7

(1) No aggregate under the slab, No SSD system.
(2) Aggregate under the slab, No SSD system.
(3) Aggregate and membrane beneath aggregate with 1 cm gap at the footers, No SSD system.
(4) Same as (3) With SSD system operating at -60 Pa.
(5) Same as (2) With SSD system operating at -60 Pa.

Soil permeability : $10^{-9}\ m^2$
Aggregate permeability : $2.0 \times 10^{-8}\ m^2$
C_∞ is the soil-gas radon concentration far from the soil surface and the substructure.

Discussion

Based on this limited assessment for a specific soil and aggregate permeability, installation of a membrane beneath subslab aggregate with a 1 cm wide gap at the periphery of the membrane has two benefits. First, SSV performance is enhanced. Second, the membrane partially counteracts the increase in radon entry due to installation of aggregate. We speculate that a membrane will, in some situations, fully counteract the increase in radon entry due to the selection of a more permeable aggregate. These findings are only tentative. Further analysis are required to evaluate the impact of membranes for other soil and aggregate permeabilities and with different sizes and locations of openings in the membrane.